



LAWRENCE  
LIVERMORE  
NATIONAL  
LABORATORY

# Chemically Specific Cellular Imaging of Biofilm Formation

J. L. Herberg, C. Schaldach, J. Horn, E. Gjersing,  
Robert Maxwell

February 10, 2006

## **Disclaimer**

---

This document was prepared as an account of work sponsored by an agency of the United States Government. Neither the United States Government nor the University of California nor any of their employees, makes any warranty, express or implied, or assumes any legal liability or responsibility for the accuracy, completeness, or usefulness of any information, apparatus, product, or process disclosed, or represents that its use would not infringe privately owned rights. Reference herein to any specific commercial product, process, or service by trade name, trademark, manufacturer, or otherwise, does not necessarily constitute or imply its endorsement, recommendation, or favoring by the United States Government or the University of California. The views and opinions of authors expressed herein do not necessarily state or reflect those of the United States Government or the University of California, and shall not be used for advertising or product endorsement purposes.

## **Chemically Specific Cellular Imaging of Biofilm Formation**

**Tracking Number:** 05-ERD-026

**Principal Investigator:** Julie L. Herberg (CMS)

**Co-Investigators:** Charlene Schaldach (CMS), Joanne Horn (CMS), Erica Gjersing (CMS), Robert Maxwell (CMS)

### **Overview:**

This document and the accompanying manuscripts summarize the technical accomplishments for our one-year LDRD-ER effort.

Biofilm forming microbes have existed on this planet for billions of years and make up 60% of the biological mass on earth. Such microbes exhibit unique biochemical pathways during biofilm formation and play important roles in human health and the environment. Microbial biofilms have been directly implicated in, for example, product contamination, energy losses, and medical infection that cost the loss of human lives and billions of dollars. In no small part due to the lack of detailed understanding, biofilms unfortunately are resistant to control, inhibition, and destruction, either through treatment with antimicrobials or immunological defense mechanisms of the body. Current biofilm research has concentrated on the study of biofilms in the bulk. This is primarily due to the lack of analytical and physical tools to study biofilms non-destructively, in three dimensions, and on the micron or sub-micron scale. This has hindered the development of a clear understanding of either the early stage mechanisms of biofilm growth or the interactions of biofilms with their environment.

Enzymatic studies have deduced a biochemical reaction that results in the oxidation of reduced sulfur species with the concomitant reduction of nitrate, a common groundwater pollutant, to dinitrogen gas by the bacterium, *Thiobacillus denitrificans* (*TD*). Because of its unique involvement in biologically relevant environmental pathways, *TD* is scheduled for genome sequencing in the near future by the DOE's Joint Genome Institute and is of interest to DOE's Genomes to Life Program. As our ecosystem is exposed to more and more nitrate contamination large scale livestock and agricultural practices, a further understanding of biofilm formation by organisms that could alleviate these problems is necessary in order to protect our biosphere. However, in order to study this complicated organism, we needed to first turn our attention to a well understood organism. *Pseudomonas aeruginosa* (*PA*) is a well-studied organism and will be used to compare our results with others. Then, we will turn our attention to *TD*. It is expected that the research performed will provide key data to validate biochemical studies of *TD* and result in high profile publications in leading journals.

For this project, our ultimate goal was to combine both Magnetic Resonance Imaging (MRI) and Nuclear Magnetic Resonance (NMR) experimental analysis with computer simulations to provide unique 3D molecular structural, dynamics, and functional information on the order of microns for this DOE mission relevant microorganism, *T. denitrificans*. For FY05, our goals were to: (1) Determine proper media for optimal growth of *PA*; growth rate measurements in that media and characterization of metabolite signatures during growth via <sup>1</sup>H and <sup>13</sup>C NMR, (2) Determine and build mineral, metal, and implant material surfaces to support growth of *PA*, (3) Implementing new MRI sequences to image biofilms more efficiently and increase resolution with new hardware design, (4) Develop further diffusion and flow MRI measurements of biofilms and biofilm formation with different MRI pulse

sequences and different hardware design, and (5) Develop a zero dimension model of the rate of growth and the metabolite profiles of *PA*. Our major accomplishments are discussed in the following text. However, the bulk of this work is described in the attached manuscript entitled, "NMR Metabolomics of Planktonic and Biofilm Modes of Growth in *Pseudomonas aeruginosa*." This paper will be submitted to the Journal of Bacteriology in coming weeks. In addition, this one-year effort has led to our incorporation into the Enhanced Surveillance Campaign during FY05 for some proof-of-principle MRI measurements on polymers. We are currently using similar methods to evaluate these polymers. In addition, this work on MRI measurements on polymers has led to a paper entitled, "Characterization of local deformation in filled-silicone elastomers subject to high strain NMR MOUSE and Magnetic Resonance Imaging as a diagnostic tool for detection of inhomogeneities." This paper has been accepted to the journal Polymer Degradation and Stability.

### **Chemically Specific Cellular Imaging of Biofilm Formation**

For this project, our accomplishments include:

1. **Preparation of unlabeled and isotopically labeled *Pseudomonas aeruginosa* (*PA*)** - We have been successful in growing *PA* biofilms in a reactor. This was the first necessary step to ensure the future success of this proposal. The bulk of this data is discussed in the attached paper entitled "NMR Metabolomics of Planktonic and Biofilm Modes of Growth in *Pseudomonas aeruginosa*."
2. **Determining and building mineral, metal, and implant material surfaces to growth *PA*** - We have grown *PA* on both glass and plastic. Glass and plastic surfaces are good model systems for environmental and medical relevant conditions. This knowledge has allowed us to grow *PA* biofilms within an MRI probe housing for direct imaging (see 3, below).
3. **Developing and implementing diffusion and flow MRI measurements of biofilms and biofilm formation**- We have successfully developed techniques to measure both flow and diffusion through the biofilm. This is shown in Figure 1.
4. **Image *PA* with our current MRI system** We have been successful in imaging biofilms and have obtained resolutions on the order of 12x12x16 $\mu$ m. Figure 2 shows a plant stem with a resolution of 12 $\mu$ m x 12 $\mu$ m x 2mm and seed beads broken in half and surrounded by Omniscan doped water with a resolution of 12 x 12 x 16  $\mu$ m/pixel. In addition, we have obtained two and three dimensional MR Images of *PA*. This is shown in Figure 3 and 4.
5. **Performing  $^1\text{H}$  and  $^{13}\text{C}$  NMR spectroscopy to examine the metabolite signatures and developing the zero dimension model of the rate of growth** - Initial  $^1\text{H}$  and  $^{13}\text{C}$  NMR spectra of labeled and unlabeled samples have been obtained. These spectra are unbiased, quantitative chemical inventories of the time dependent metabolite pool. We have established parameters to perform the *in-situ* time dependent  $^1\text{H}$  and  $^{13}\text{C}$  NMR on *PA* to watch the metabolite signatures

during the growth stage. We used Principle Component Analysis (PCA) to develop a zero dimensional growth model. This is again discussed in the attached paper entitled "NMR Metabolomics of Planktonic and Biofilm Modes of Growth in *Pseudomonas aeruginosa*."

*Work was performed under the auspices of the U.S. Department of Energy by Lawrence Livermore National Laboratory under contract number W-7405-ENG-48. The project (05-ERD-026) was funded by the Laboratory Directed Research and Development Program at LLNL.*

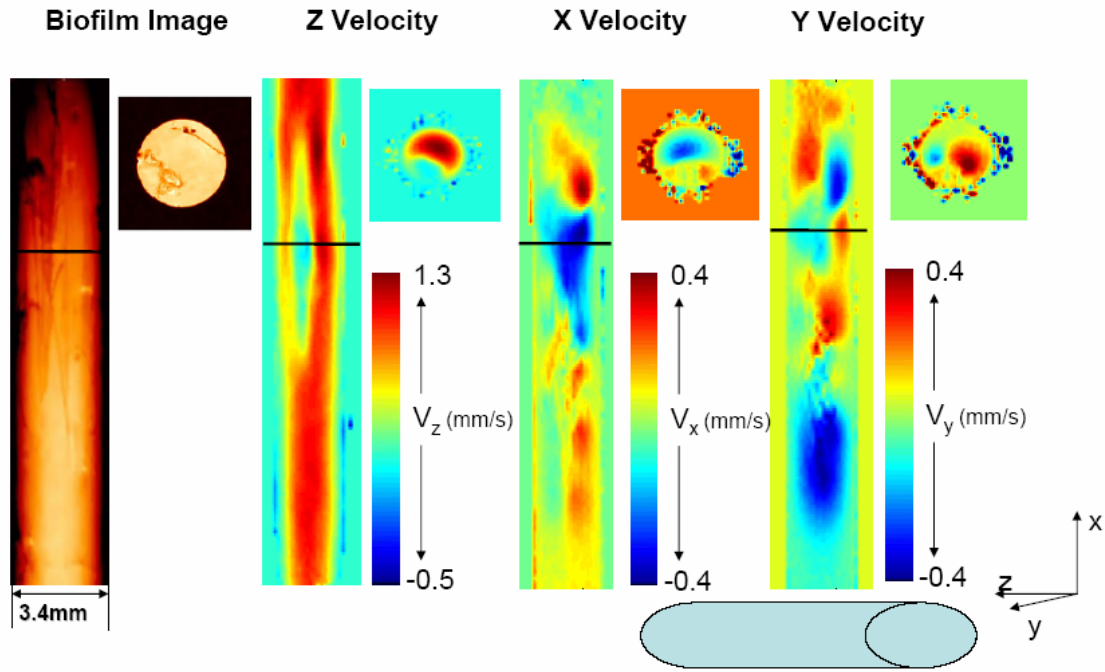
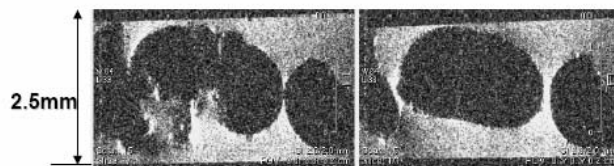


**Figure 1:** MRI flow and diffusion measurements on *P. aeruginosa* biofilm

Seed beads broken in half and surrounded by Omniscan doped water



12 x 12 x 16 micron/pixel  
Exp. Time = 22 hrs  
Aves = 4



Obtained high resolution MR Image of a plant stem 12  $\mu\text{m}$  x 12  $\mu\text{m}$  x 2mm

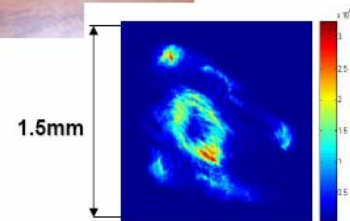


**Figure 2:** MRI images of Seed beads broken in half and surrounded by Omniscan doped water with a resolution of 12 x 12 x 16  $\mu\text{m}$ /pixel and plant stem with a resolution of 12  $\mu\text{m}$  x 12  $\mu\text{m}$  x 2mm.

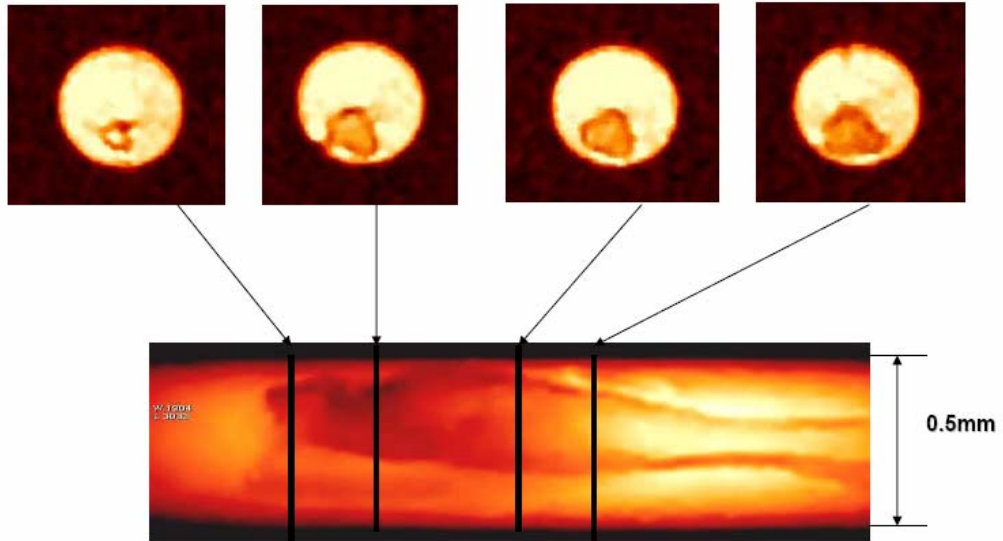
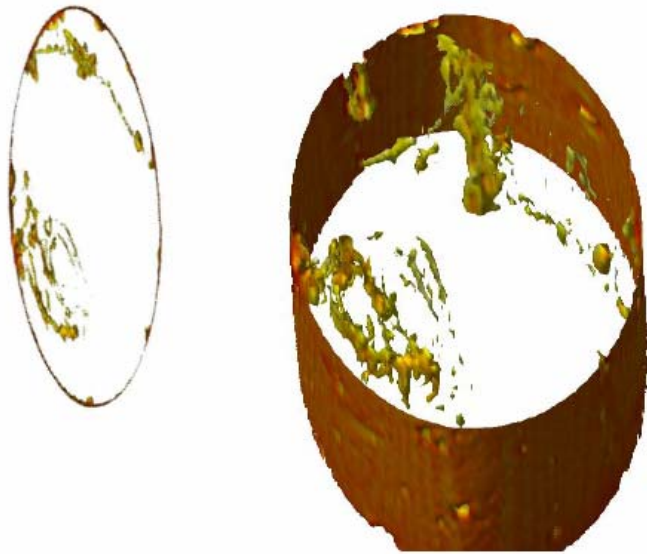


**Figure 3:** MR Images of *PA* biofilm with resolution 20 x 20 x 39  $\mu\text{m}$ /pixel.



**Resolution: 27 x 27 x 55  $\mu\text{m}/\text{pixel}$**

**Figure 4:** 3D MR Image of *PA* Biofilm with resolution of 27 x 27 x 55  $\mu\text{m}/\text{pixel}$ .

## **NMR Metabolomics of Planktonic and Biofilm Modes of Growth in *Pseudomonas aeruginosa***

Erica Gjersing, Julie Herberg<sup>\*</sup>, Joanne Horn, Charlene Schaldach, Robert Maxwell  
*Chemistry and Materials Science Directorate, Lawrence Livermore National Laboratory*

### **ABSTRACT**

Bacteria often reside in communities where the cells have secreted a sticky, polysaccharide substance, which allows them to attach to surfaces. This sessile lifestyle referred to as a biofilm, affords the cells within these communities a tolerance of antibiotics and antimicrobials treatments. Biofilms of the bacteria *Pseudomonas aeruginosa* are capable of infecting medical implant devices, such as heart valves and catheters, where treatment of the infection often requires the removal of the infected device. This mode of growth is in stark contrast to planktonic, free floating cells which are easily eradicated with antibiotics. The mechanisms contributing to a biofilm's tenacity and a planktonic cell's vulnerability are just beginning to be explored.

In this study, we have used NMR metabolomic techniques to study the metabolic distinctions between these two modes of growth in *P. aeruginosa* bacteria. One-dimensional proton spectra of fresh growth media was compared with media supernatants from planktonic and biofilm cultures. In addition, high resolution magic angle spinning (HRMAS) techniques were employed to collect proton NMR spectra of the cells themselves. Principal component analysis and spectral comparisons revealed that the overall metabolism of planktonic and biofilm modes of growth is similar, but the cells themselves display marked differences.

**KEYWORDS:** Nuclear Magnetic Resonance (NMR), Solid State Magic Angle Spinning  
NMR, HRMAS, biofilm, metabolomics, principle component analysis

\*Corresponding author. Mailing address: 7000 East Avenue, Livermore, Ca 94550, Tel:  
+1-925-422-5900, Fax: +1-925-422-5565, Email: herberg1@llnl.gov

## INTRODUCTION

Bacteria, such as *Pseudomonas aeruginosa*, often reside in communities called biofilms that are attached to surfaces and encase themselves in a polysaccharide matrix. *P. aeruginosa* biofilms have been implicated in cystic fibrosis and nosocomial infections where they are of major concern due to their tolerance of antibiotics (7, 33). An understanding of the mechanisms involved in a biofilm's ability to withstand antimicrobials is needed to develop new methods of treatment (9). Comparisons of biofilm cells to their planktonic counterparts have already begun to allude to the many factors involved in a biofilm's ability to withstand antimicrobials. So far, significant proteomic differences have been discovered for *P. putida*, when this bacteria is grown in suspended cultures versus a sessile mode (29), and throughout the development of a *P. aeruginosa* biofilm (30). In addition, changes in expression have been discovered in genes involved in motility, quorum sensing and polysaccharide production (8, 27, 40).

The metabolome, defined as the inventory of all the metabolites in a biological system (13), is akin to the proteome and genome. Genetic regulation can cause changes in protein expression and activity from those proteins should be observed in the metabolites (14). Metabolome data is useful in a variety of applications all with the ultimate goal of understanding cause and effect processes within biological systems. As a functional genomics tool, metabolite concentrations have been used to expose phenotypes in yeast mutants (28) and plants (39), which, based on growth rates and fluxes, appear to be identical. Metabolome analysis has also proven useful in measuring metabolite responses to stress such as disease in abalone (37), and growth rate (36) and culture densities (23) in *Escherichia coli*. Biological samples used for metabolomics can

include a variety of biofluids such as urine, serum, blood, or bile for human and animal subjects (22, 25) while plant and microorganism studies are conducted on cells (2, 5), cell extracts (12), or growth media supernatants (3). Due to the diversity of metabolites and the range of concentrations, identifying all the components of the metabolome, even for simple microorganisms, has proven difficult.

Nuclear Magnetic Resonance (NMR) spectroscopy is a technique that can provide overall profiles of all the metabolite species within a crude sample in a non-destructive manner without extensive preparation procedures (12). One of the drawbacks to NMR is the sensitivity of the technique which, in some cases, may not detect low concentration metabolites. Additional processing, such as pattern recognition techniques, are often needed in order to gather the useful information from the NMR spectra of crude samples because so many different chemical species (i.e. NMR peaks) are present (21), (38) (10) (19). Despite these aspects, NMR-based metabonomics has found applications in a variety of areas. Bodily fluids from both humans and animals are routinely screened in the drug-discovery field in order to develop methods for disease diagnosis (18, 25). In addition, the NMR metabolite “fingerprints”, the overall profile of metabolites, have been used to distinguish between different species of bacteria (1, 11, 17) and also between strains of the same bacteria (4, 26).

A useful NMR technique for studying semi-solid samples, such as cells, is High Resolution Magic Angle Spinning (HRMAS). Samples are spun around their own axis at speeds between 4-12 kHz and at an angle of  $54.7^\circ$  relative to the external magnetic field in order to reduce linewidths by averaging out chemical shift anisotropy, magnetic susceptibility, and dipolar coupling (15). This technique has been used to distinguish

between healthy and diseased human tissue samples (6, 24) and to determine chemical compositions of algal cells (2, 5, 34). New HRMAS NMR methods using lower spin rates have been tested on *Shewanella oneidensis* biofilms (20). Tomlins et. al. (35) found HRMAS to be extremely useful in the identification of metabolites in prostate tissue, and concluded that HRMAS provides more information than typically used metabolite extraction procedures.

The work presented in this paper demonstrates the use of NMR based metabolite identification techniques to characterize crude samples of *P. aeruginosa* in both the planktonic and biofilm states. Traditional liquid state NMR spectroscopy is used to characterize the media that the cells were cultured in to determine differences in excreted metabolites and in media metabolism. In addition, HRMAS techniques were used to determine the chemical composition of the cells themselves for the two phenotypes. Finally, principle component analysis (PCA) was utilized to investigate the statistical significance of the differences between the NMR spectra.

## **MATERIALS AND METHODS**

**Planktonic culture.** *Pseudomonas aeruginosa* strain PAO1 was grown from freezer culture on Luria-Bertani (LB) agar plates. Planktonic cultures were grown from a single colony inoculated in 50 mL LB media and continuously stirred at 37°C for 16 hours

**Biofilm culture.** To cultivate biofilm samples, a 3 mL slug of a planktonic culture, grown as described above, was injected from downstream into a one meter length of silicon tubing with an internal diameter of 3/32" (Cole-Palmer) and allowed to sit

under static conditions for 4 hours. LB media was then pumped through at a rate of 0.15mL/min for 48 hours. Both inoculation and flow-through cultivation were carried out in an incubator at 37°C. A media flow-break was placed upstream from the tubing to prevent contamination of the media fluid reservoir. The biomass was harvested in a similar manner to that described by Sauer and Camper (29) for protein analysis, where the tubing was pinched to dislodge the biofilm then purged with filtered air and the sample collected in a centrifuge tube.

**Luria-Bertani Media.** The LB media was prepared with 10 grams tryptone (Bacto), 5 grams yeast extract (SigmaEZ), and 5 grams NaCl per liter of deionizer water and autoclave sterilized.

**Liquid sample preparation for NMR spectroscopy.** To prepare samples for traditional liquids NMR analysis, 25 mL of planktonic culture and each of the 1 mL sections from the biofilm cultures were centrifuged for 5 minutes which pulled the cells to the bottom and left liquid supernatant. A 0.5mL aliquot of liquid supernatant or LB media was aseptically extracted from the centrifuge tube or bottle and placed in an NMR tube. This sample was then frozen until NMR experiments were performed. Prior to acquiring the spectra, 0.5mL of D<sub>2</sub>O + 0.2%v tetramethylsilane (TMS) was added to the NMR tube for locking and referencing.

**HRMAS sample preparation.** The remaining liquid supernatant was removed from the centrifuge tube and 0.5 mL D<sub>2</sub>O was added and tube was vortex for approximately 5 seconds to suspend the cells. The tube was then centrifuged for 5 minutes and the liquid pulled off. This procedure was repeated two more times fully rinse any remaining liquid supernatant from the cells. The cell pellets were kept in the

centrifuge tubes and refrigerated until the HRMAS NMR experiments could be performed (approximately 3 weeks). Each cell sample was made directly before the HRMAS NMR experiments could be performed by filling an 4 mm HRMAS rotor (Bruker Biospin) with the refrigerated cells. Since the cell samples were washed in D<sub>2</sub>O, there was enough residual left for deuterium locking. TMS was not added to these samples. Cell samples were streaked on LB agar plates prior to and after running the HRMAS NMR experiments and the cells were viable in both instances.

**Liquid Supernatant NMR Experiments.** All proton NMR spectra were acquired at 500.0894 MHz on a Bruker Avance spectrometer at ambient temperature. A 5mm Bruker BBO probe was used to acquire liquid supernatant spectra. Water suppression was accomplished using a presaturation pulse sequence. For each spectrum 64k data points were collected for 128 transients over a spectral width of 6775 Hz. All spectra were manually phase corrected and referenced to TMS at 0 ppm.

**HRMAS NMR experiments.** HRMAS NMR spectra were acquired with a SB BL4 probe with z-gradients while spinning at 5 kHz. Presaturation water suppression was used to minimize the large water signal. For each sample 64k data points were collected with 1000 scans and a recycle delay of 5 sec. The spectra were manually phase corrected and externally referenced to TMS.

**Data Processing and Principle Component Analysis.** The same analysis was used for both the liquid supernatant and HRMAS spectra. The spectral region from 10 to 0 ppm was divided into equal “buckets” of 0.04 ppm using AMIX software (version 3.0.1, Bruker Biospin). The region from 4.5-6 was not included so that the variability of the suppressed water signal would not interfere with the statistical analysis, which is shown

in Figure 1. The integrated intensities were saved as an ASCII file and loaded as matrices into MatLab (version 7.0.4, MathWorks). The MatLab Statistics Toolbox (version 7.0.4, MathWorks) was used to perform principle component analysis. All PCA and spectra plots were generated using MatLab.

## RESULTS

**Liquid Supernatant.** Biofilm samples were prepared from three bioreactors and each reactor was divided equally into three sections with an approximate volume of 1mL. The first section was designated as the section closest to the fresh media inlet, the second being from the middle of the reactor and the third closest to the outlet. For the analysis presented here, the samples will be referred to as BF for biofilm, followed by the reactor number then the section number, so a sample taken from the first reactor, first section will be designated as BF1-1, second section BF1-2, and third section BF1-3. Three planktonic cultures were used for this analysis and two samples were collected from each culture. Planktonic samples will be referred to by the culture number first followed by the sample number, with a PL preceding. Therefore, the first sample from the first culture will be PL1-1 and the second sample is PL1-2. Nine samples of LB media were collected, each from a different container that had been measured out and prepared separately.

Representative NMR spectra for LB media, biofilm and planktonic supernatant are shown in Figure 2. Biofilm sample BF2-2 is presented along with planktonic sample PL1-1. The TMS reference peak at 0 ppm is shown in both the planktonic and LB media spectra, but is not present in the biofilm supernatant. Only one biofilm sample, BF3-3

displayed a peak at 0 ppm but the intensity of the peak was much smaller than for the planktonic and LB media spectra. All the samples were prepared with the same solution of D<sub>2</sub>O + TMS and handled in exactly the same manner, so it appears that the TMS must have been broken down in the biofilm supernatant. The pH of all the samples was tested and found to be in the range of 7-8, in addition there does not appear to be any significant shifts in the NMR peaks to indicate a difference in pH. Therefore, it is not possible that strong acids or bases reacted with the TMS. This leaves two possibilities: 1) a strong oxidizing agent being present in the biofilm supernatant or 2) a reaction occurred due to the presence of some silicone compound that leached into liquid from the silicone tubing used to cultivate the biofilm samples.

The overlays of the spectra in Figure 2 demonstrate that each of the spectra is visually distinct from the others. In order to demonstrate that the spectra are all statistically different from each other principle component analysis (PCA) was performed. The score plot displayed in Figure 3 shows that the samples from the LB media, planktonic and biofilm supernatant are all contained within separate groupings. The first principal component (PC) separates the LB media from the supernatant samples and accounts for 45% of the variability in the data. Another 33% of the variability is described by the second PC which isolates the planktonic samples from the LB and biofilm samples. An additional PC, not shown, describes 12% of the variation, so that the 90% of the variation in the data is described by three principle components.

From Figure 4 it can be seen that most of the variation between the biofilm and planktonic spectra occurs due to higher peak intensities in the planktonic supernatant. Specifically, the cell byproduct of acetate at 1.92 ppm (12) appears to have a stronger

intensity, and therefore higher concentrations, in the planktonic culture. This higher intensity appears to be an artifact from the experimental setup where the planktonic samples were grown in batch culture, allowing cell byproducts to build up within the system. In contrast, the biofilm samples were grown in a flow through where cell byproducts were flushed away and diluted with fresh media. There does not appear to be any new or novel peaks present in either of the samples relative to each other, with the exception of the TMS peak being present in the planktonic and not in the biofilm samples.

**HRMAS NMR of Cells.** While the supernatant from each of the cultures was analyzed by liquids state NMR spectroscopy, the cells themselves were investigated with HRMAS solid-state NMR spectroscopy. The same sample naming scheme is used for the cells that was used for the supernatant samples. One cell sample was run from each of the three sections in the three biofilm reactors for a total of 9 biofilm samples. Three planktonic cell samples, one from each of the supernatant samples, were investigated.

One of the main concerns with setting up experiments on whole cells was sample preparation and storage. Preliminary studies conducted in our laboratory indicated that the HRMAS spectra were very sensitive to differing magnet conditions (i.e. natural drifts in magnetic fields). Initially spectra were collected a week or two apart from each other and the magnet shimming was adjusted during that time or the probe removed for liquids experiments. PCA analysis on these spectra revealed grouping based on the date that the spectra were acquired rather than the sample. In order to investigate this potential artifact in the data, the cell samples were collected and stored over the course of two weeks. The spectra for all the samples were then collected over the course of a few days, without

removing the probe or extreme changes in the shimming. The results of these measurements are presented in this paper.

Figure 5 displays representative HRMAS spectra from planktonic culture PL3 and biofilm sample BF2-3. The expanded regions, the middle and bottom plots, show that significant differences, not just peak intensities as in the liquid NMR spectra, are found between the two spectra. This data clearly shows that the planktonic and biofilm cell samples display distinctly different HRMAS NMR peaks. The center plot of Figure 5 shows that the planktonic culture displays peaks at 6.59 ppm and 7.87 ppm that are not found in the biofilm cells. The bottom plot of Figure 5 displays many areas where the planktonic sample has higher peak intensity, most notably at 1.74 ppm, 3.02 ppm, 3.25 ppm and from 3.5-4 ppm. However, the peak at 2.33 ppm appears higher in the biofilm spectra. The NMR peak at 2.33 ppm is most likely the acetyl group of alginate (31) which is produced in large quantities in *P. aeruginosa* biofilms. The original reference for this peak is at 2.13 ppm. The shift from 2.33 to 2.13 ppm is most likely due to the fact that, for our work, spectra were acquired at 25°C while the reference was at 92°C. There are additional resonance peaks reported by the reference, between 3.73–5.36 ppm. However, because of the water suppression scheme, which will also suppress protons that are exchanging with the water, and the removal of all resonances between 4-6 ppm for PCA, these peaks are not seen in the data presented here.

The PCA score plot in Figure 6 shows that the cell samples divide into two distinct and widely separated groupings based on the first PC which describes 60% of the variation within the data set. The second PC, which accounts for 15% of the variation within the data, describes the wide variation in the biofilm samples. This plot also

separates out one of the biofilm reactors, BF1 circled in light grey, from the other two. The separation is most likely due to the fact that Reactors 2 and 3 were grown in parallel and BF1 was grown a week prior.

## **DISCUSSION**

The choice of reactor set up and sample preparation proved to be the most significant factor in the differences observed from the media supernatants. In previous studies comparing biofilm and planktonic cells, chemostats have been employed to ensure that the cells experience the same environment. With this method the biofilm is cultivated on a surface inside a reactor which also contains suspended cells. For our work we wanted to study the media of the two cells types which required separate cultivations. However, the separate reactors produced artifacts in the data since the biofilm media was continually refreshed whereas, in the planktonic batch culture, by products were allowed to build up. This artifact could possibly be remedied with the use of a chemostat for cultivation of the planktonic cells where the dilution rate is matched to that of the biofilm system.

Despite this artifact, the spectra for the two types of cells appear markedly similar. From this analysis, it appears that the overall metabolism in a biofilm system is quite similar to that of planktonic cultures. This result is not unexpected since it is known that cells have various, stratified growth rates throughout the depth of a biofilm. The cells in the system which are at the biofilm-liquid interface cover the most surface area and have the highest growth rates and most active metabolism (9). Therefore, it is these cells which would contribute the most significant amount of metabolites in an investigation of

the growth media. Previous studies have shown that these surface cells are as susceptible to antimicrobial treatment as planktonic cells (16, 32). This combined evidence indicates that the cells on the biofilm-liquid interface are utilizing the same metabolic pathways as suspended cells.

The real differences between planktonic and biofilm modes of growth was seen when the cells themselves were studied by HRMAS NMR. The 1-D  $^1\text{H}$  NMR spectra presented in this paper are far too complex to identify all the individual compounds within the two systems; however, they still demonstrate the distinct nature of the two types of cells. It should be noted that due to the sample preparation procedures, of washing the cells to remove any media, and the refrigerator storage, that the cells were under stress at the time the NMR spectra were collected. Investigating the stress response of cells to environmental stimuli is the goal of metabolomics and this study presents just one of the thousands of possible instances that could be investigated. Additional studies into the best sample preparation procedures should be undertaken.

The PCA analysis of the HRMAS NMR spectra clearly shows the statistical significance of the differences between the planktonic and biofilm cells, with 60% of the difference described by the first PC. The second PC, which describes the spread in the biofilm samples, is also quite significant at 15%. This result is most likely indicative of the varied physiological states within a biofilm, from anaerobic at the center of clusters to high growth rates zones at the liquid interface. In contrast, the planktonic samples, which are assumed to be homogenous, form a tight grouping.

It was expected that the variation in the biofilm samples would separate based on the reactor that the samples were grown in or by section of reactor. Since the biofilm

growth setup is essentially a plug flow reactor, the beginning sections of tubing should have higher concentrations of nutrients while the later sections should have higher concentrations of by products. The cell sample PCA (Figure 6) did show a separation of one of the reactors, however, no groupings are apparent in the supernatant sample PCA (Figure 3). The obvious answer to the lack of clear separation between the different sections of reactor would be to assume that significant mixing occurs during the harvesting procedure which homogenizes the samples. However, if this were the case, all the reactors should cluster together much more readily than is apparent by either the supernatant or cell data. Therefore, these results seem to reflect true heterogeneity both along the length of the biofilm reactor system and between the reactors. A more in-depth study of the causes and conditions involved in this heterogeneity should be undertaken in the future.

This study has shown that in order to conduct NMR based metabolomic studies on biofilm systems HRMAS NMR will have to be employed rather than liquid state NMR of the media supernatants. The true utility of this type of work will become more evident when combined with proteomic and genomic data. However, due to the vast variation in biofilm systems under different growth conditions, this type of work will most certainly have to be performed on a single, integrated system. The work presented in this paper represents one small piece of a much larger puzzle that will eventually form a picture of the metabolic responses of biofilm and planktonic cells to environmental factors.

## ACKNOWLEDGMENTS

Work was performed under the auspices of the U.S. Department of Energy by Lawrence Livermore National Laboratory under contract number W-7405-ENG-48. The project (05-ERD-026) was funded by the Laboratory Directed Research and Development Program at LLNL.

## REFERENCES

1. **Bourne, R., U. Himmelreich, A. Sharma, C. Mountford, and T. Sorrell.** 2001. Identification of *Enterococcus*, *Streptococcus*, and *Staphylococcus* by multivariate analysis of proton magnetic resonance spectroscopic data from plate culture. *J. of Clin. Microbiol.* **39**:2916-2923.
2. **Broberg, A., and L. Kenne.** 2000. Use of high-resolution magic angle spinning nuclear magnetic resonance spectroscopy for *in situ* studies of low-molecular-mass compounds in red algae. *Anal. Biochem.* **284**:367-374.
3. **Bubb, W. A., L. C. Wright, M. Cagney, R. T. Santangelo, T. C. Sorrell, and P. W. Kuchel.** 1999. Heteronuclear NMR studies on metabolites produced by *Cryptococcus neoformans* in culture media: Identification of possible virulence factors. *Magn. Reson. Med.* **42**:442-453.
4. **Bundy, J. G., T. L. Willey, R. S. Castell, D. J. Ellar, and K. M. Brindle.** 2005. Discrimination of pathogenic clinical isolates and laboratory strains *Bacillus cereus* by NMR-based metabolic profiling. *FEMS Microbiol. Lett.* **242**:127-136.

5. **Chauton, M. S., T. R. Storseth, and G. Johnsen.** 2003. High-resolution magic angle spinning  $^1\text{H}$  NMR analysis of whole cells of *Thalassiosira pseudonona* (Bacillariophyceae): Broad range analysis of metabolic composition and nutritional value. *J. of Appl. Phycol.* **15**:533-542.
6. **Cheng, L. L., M. J. Ma, L. Becerra, T. Ptak, I. Tracey, A. Lackner, and R. G. Gonzalez.** 1997. Quantitative neuropathology by high resolution magic angle spinning proton magnetic resonance spectroscopy. *Proc. Natl. Acad. Sci.* **94**:5408-6413.
7. **Costerton, J. W., P. S. Stewart, and P. E. Greenburg.** 1999. Bacterial biofilms: A common cause of persistent infections. *Science* **284**:1318-1322.
8. **Davey, M. E., and G. A. O'Toole.** 2000. Microbiofilms: from ecology to molecular genetics. *Microbiol. Mol. Bio. Rev.* **64**:846-847.
9. **Davies, D.** 2003. Understanding biofilm resistance to antibacterial agents. *Nat. Rev. Drug Discov.* **2**:114-122.
10. **Daykin, C. A., J. P. M. Van Duynhoven, A. Groenewegen, M. Dachtler, J. M. M. Van Amelsvoort, and T. P. J. Mulder.** 2005. Nuclear magnetic resonance spectroscopic based studies of the metabolism of black tea polyphenols in humans. *J. Agric. Food Chem.* **53**:1428-1434.
11. **Delpassand, E. S., M. V. Chari, C. E. Stager, J. D. Morrisett, J. J. Ford, and M. Romazi.** 1995. Rapid identification of common human pathogens by high-resolution proton magnetic resonance spectroscopy. *J. Clin. Microbiol.* **33**:1258-1262.

12. **Fan, T. W. M.** 1996. Metabolite profiling by one- and two-dimensional NMR analysis of complex mixtures. *Progr. Nucl. Magn. Reson. Spectros.* **28**:161-219.
13. **Fiehn, O.** 2002. Metabolomics- the link between genotypes and phenotypes. *Plant Mol. Biol.* **48**:155-171.
14. **Fiehn, O., S. Kloska, and T. Altmann.** 2001. Integrated studies on plant biology using multiparallel techniques. *Curr. Opin. Biotech.* **12**:82-26.
15. **Fukushima, E., and S. B. W. Roeder.** 1981. *Experimental Pulse NMR: A Nuts and Bolts Approach.* Addison-Wesley Publishing Company, Inc., Reading, Massachusetts.
16. **Fux, C. A., J. W. Costerton, P. S. Stewart, and P. Stoodley.** 2005. Survival strategies of infectious biofilms. *Trends Microbiol.* **13**:34-40.
17. **Garg, M., M. K. Misra, S. Chawla, K. N. Prasad, R. Roy, and R. K. Gupta.** 2003. Broad identification of bacterial type from pus by <sup>1</sup>H MR spectroscopy. *Euro. J. Clin. Investig.* **33**:518-524.
18. **Griffin, J. L.** 2003. Metabonomics: NMR spectroscopy and pattern recognition analysis of body fluids and tissues for characterization of xenobiotic toxicity and disease diagnosis. *Curr. Opin. Chem. Biol.* **7**:648-654.
19. **Holmes, E., J. K. Nicholson, A. W. Nicholls, J. C. Lindon, S. C. Connor, S. Polley, and J. Connelly.** 2003. The identification of novel biomarkers of renal toxicity using automatic data reduction techniques and PCA of proton NMR spectra of urine. *Chemometr. Intell. Lab. Syst.* **44**:245-255.
20. **Hu, J. Z., R. A. Wind, J. Mclean, Y. A. Gorby, C. T. Resch, and J. K. Fredrickson.** 2004. High-resolution <sup>1</sup>H NMR spectroscopy of metabolically

- active microorganisms using non-destructive magic angle spinning. *Spectroscopy*. **19**:98-103.
21. **Lindon, J. C., E. Holmes, and J. K. Nicholson.** 2001. Pattern recognition methods and applications in biomedical magnetic resonance. *Proc. Nucl. Magn. Reson.* **39**:1-40.
  22. **Lindon, J. C., J. K. Nicholson, E. Holmes, and J. R. Everett.** 2000. Metabonomics: Metabolic processes studied by NMR spectroscopy of biofluids. *Concepts Magn. Reson.* **12**:289-320.
  23. **Lui, X., C. NG, and T. Ferenci.** 2000. Global adaptations resulting from high population densities in *Escherichia coli* culture. *J. of Bacteriol.* **182**:4158-4164.
  24. **Moka, D., R. Vorreuther, H. Schicha, M. Spraul, E. Humpfer, M. Lipinski, P. J. D. Foxall, J. K. Nicholson, and J. C. Lindon.** 1998. Biochemical classification of kidney carcinoma biopsy samples using magic-angle spinning <sup>1</sup>H nuclear magnetic resonance spectroscopy. *J. Pharmaceut. Biomed. Anal.* **17**:125-132.
  25. **Nicholson, J. K., and I. D. Wilson.** 1989. High resolution proton magnetic resonance spectroscopy of biological fluids. *Progr. Nucl. Mag. Reson. Spectros.* **21**:449-501.
  26. **Ohara, T., I. Y., K. Itoh, and T. Tetsuka.** 2001. Analysis of methicillin-resistant *Staphylococcus aureus* isolates by proton magnetic resonance spectroscopy. *J. Infect.* **43**:116-121.
  27. **O'Toole, G. A., H. Kaplan, and R. Kolter.** 2000. Biofilm formation as microbial development. *Annu. Rev. Microbiol.* **54**:49-79.

28. **Raamsdonk, L. M., B. Teusink, D. Broadhurst, N. Zhang, A. Hayes, M. C. Walsh, J. A. Berden, K. M. Brindle, D. B. Kell, J. J. Rowland, H. V. Westerhoff, K. van Dam, and S. G. Oliver.** 2001. A functional genomics strategy that uses metabolome data to reveal the phenotype of silent mutations. *Nat. Biotechnol.* **19**:45-50.
29. **Sauer, K., and A. K. Camper.** 2001. Characterization of phenotypic changes in *Pseudomonas putida* in response to surface-associated growth. *J. of Bacteriol.* **183**:6579-6589.
30. **Sauer, K., A. K. Camper, G. D. Ehrlich, J. W. Costerton, and D. G. Davies.** 2002. *Pseudomonas aeruginosa* displays multiple phenotypes during development as a biofilm. *J. of Bacteriol.* **184**.
31. **Skjak-Braek, G., H. Grasdalen, and B. Larsen.** 1986. Monomer sequence and acetylation pattern in some bacterial alginates. *Carbohydr. Res.* **154**:239-250.
32. **Spoering, A. L., and K. Lewis.** 2001. Biofilms and planktonic cells of *Pseudomonas aeruginosa* have similar resistance to killing by antimicrobials. *J. of Bacteriol.* **183**:6746-6751.
33. **Stewart, P. S., and J. W. Costerton.** 2001. Antibiotic resistance of bacteria in biofilms. *Lancet* **358**:135-138.
34. **Storseth, T. R., K. Hansen, J. Skjermo, and J. Kranes.** 2004. Characterization of a  $\beta$ -D-(1-3)-glucan from the marine diatom *Chaetoceros mulleri* by high-resolution magic-angle spinning NMR spectroscopy on whole algal cells. *Carbohydr. Res.* **339**:421-424.

35. **Tomlins, A. M., P. J. D. Foxall, L. J.C., M. J. Lynch, M. Spraul, J. R. Everett, and J. K. Nicholson.** 1998. High resolution magic angle spinning  $^1\text{H}$  nuclear magnetic resonance analysis of intact prostatic hyperplastic and tumor tissues. *Anal. Comm.* **35**:113-115.
36. **Tweeddale, H., L. Notley-McRobb, and T. Ferenci.** 1998. Effect of slow growth on metabolism of *Escherichia coli*, as revealed by global metabolite pool ("metabolome") analysis. *J. of Bacteriol.* **180**:5109-5116.
37. **Viant, M. R., E. S. Rosenblum, and R. S. Tjeerdema.** 2003. NMR-Based Metabolomics: A powerful approach for characterizing the effects of environmental stressors on organism health. *Environ. Sci. Technol.* **37**:4982-4989.
38. **Ward, J. L., C. Harris, J. Lewis, and M. H. Beale.** 2003. Assessment of  $^1\text{H}$  NMR spectroscopy and multivariate analysis as a technique for metabolite fingerprinting of *Arbidopsis thaliana*. *Phytochemistry* **62**:949-957.
39. **Weeckwerth, W., M. Ehlers Loureiro, K. Wenzel, and O. Fiehn.** 2004. Differential metabolic networks unravel the effects of silent plant phenotypes. *Proc. Natl. Acad. Sci. Unit. States Am.* **101**:7809-7814.
40. **Whiteley, M., M. G. Banger, R. E. Bumgarner, M. R. Parsek, G. M. Teitzel, S. Lory, and P. E. Greenburg.** 2001. Gene expression in *Pseudomonas aeruginosa* biofilms. *Nature* **413**:860-864.

## **FIGURE LEGENDS**

Figure 1. Conversion of NMR spectra to “bucket” data for principle component analysis.

Figure 2: Comparison of spectra from LB media to planktonic and biofilm supernatants.

Figure 3: Principal Component Analysis Score Plot for LB media, planktonic and biofilm samples.

Figure 4: Expansion of regions of supernatant spectra demonstrating that there are very few differences in the peaks, only the intensity of the peaks is varying.

Figure 5: Representative HRMAS spectra of planktonic and biofilm cell samples.

Figure 6: PCA score plot for HRMAS spectra showing a clear separation of biofilm and planktonic cell spectra.

**FIGURE 1**

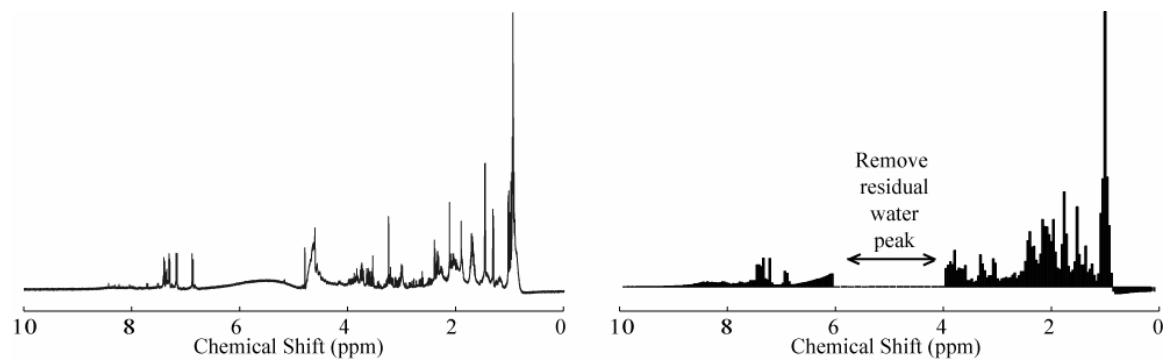
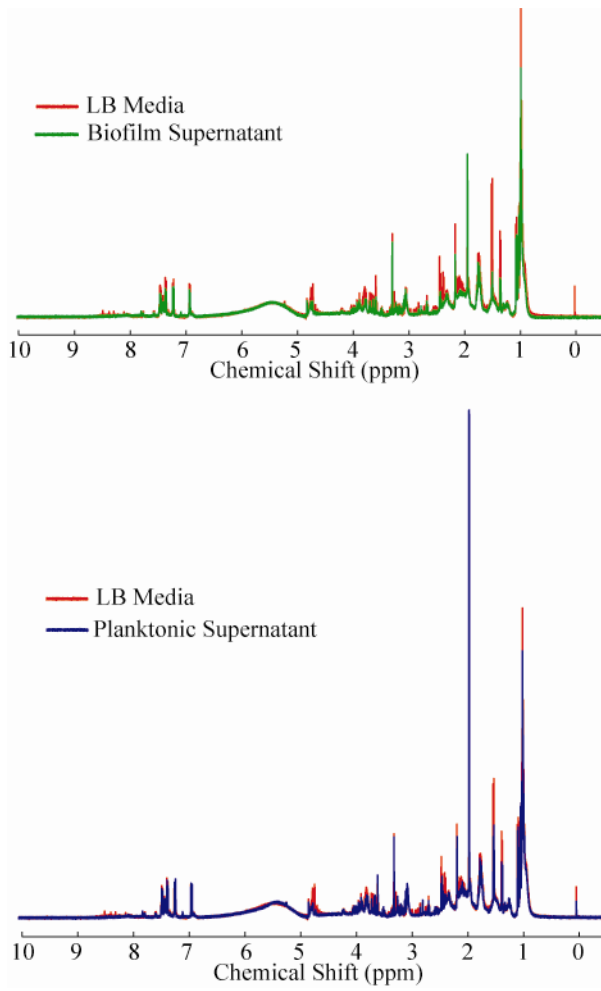
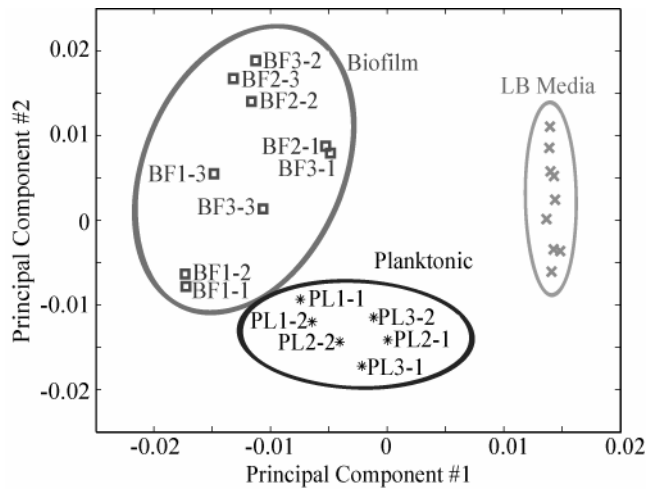


FIGURE 2



**FIGURE 3**



**FIGURE 4**

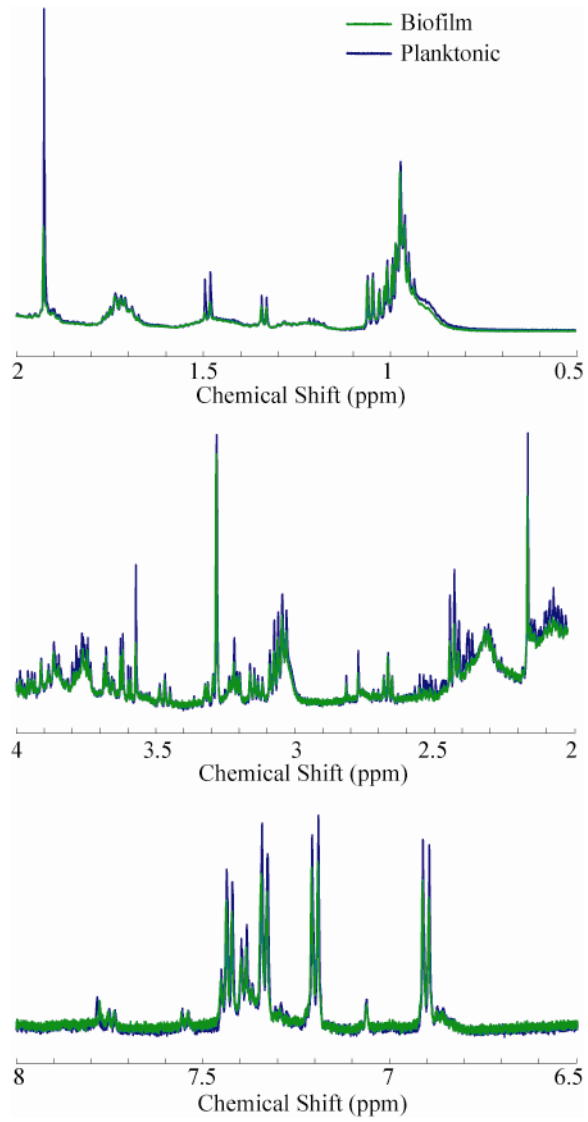


**FIGURE 5**

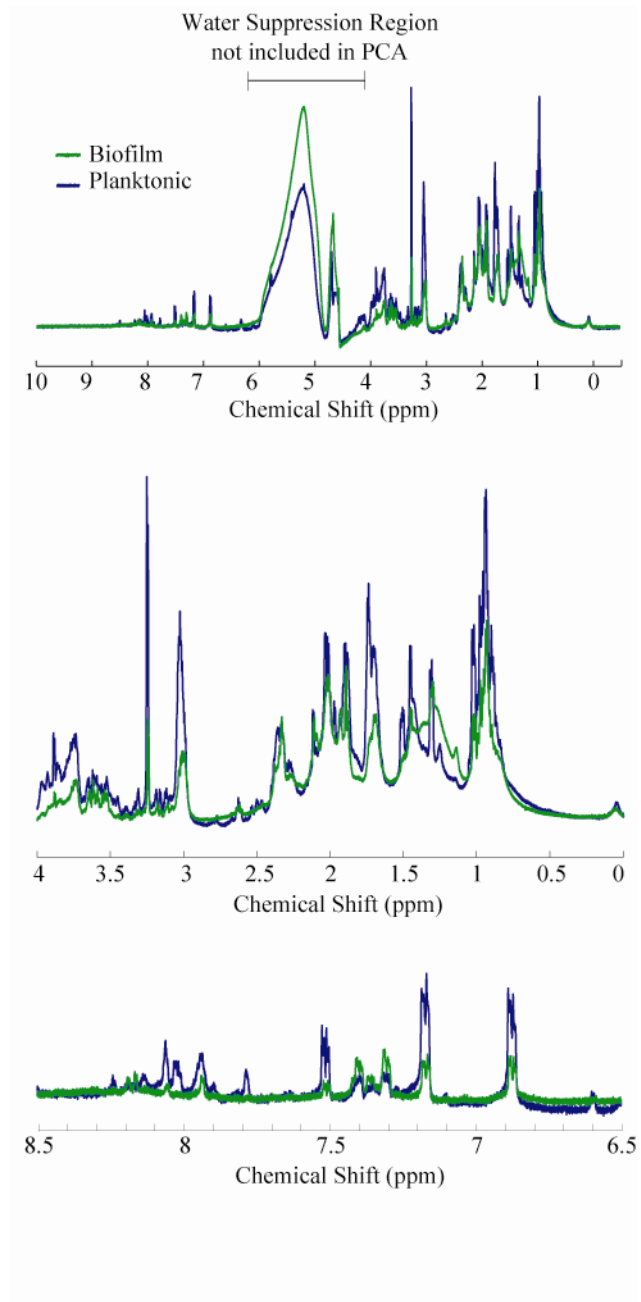
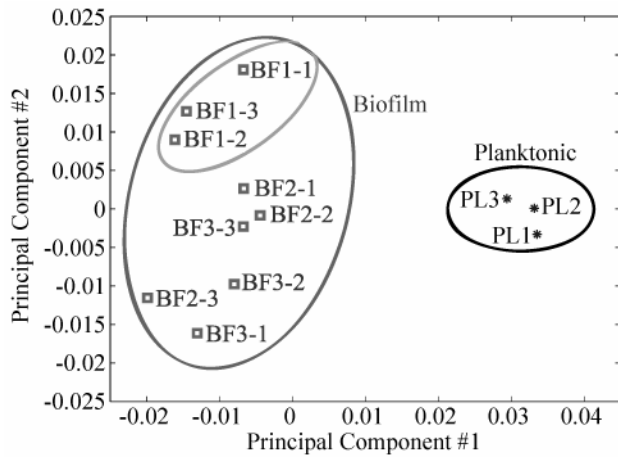


**FIGURE 6**



**Characterization of local deformation in filled-silicone elastomers  
subject to high strain - NMR MOUSE and magnetic resonance imaging  
as a diagnostic tool for detection of inhomogeneities**

Julie L. Herberg, Sarah C. Chinn, April M. Sawvel,<sup>†</sup> Erica Gjersing, and Robert S.  
Maxwell\*

*Chemistry and Materials Science Directorate*

*Livermore National Laboratory, 7000 East Avenue, Livermore, CA 94550*

***Abstract***

Magnetic Resonance Imaging (MRI) and unilateral Nuclear Magnetic Resonance (NMR) relaxometry with the NMR MOUSE (MOBILE Universal Surface Explorer) have been used to characterize local permanent deformation in silicone parts subject to high compressive strain. Samples returned from field service have been characterized by areas of high compression set. Materials excised from these damaged sections have been shown to be clearly distinguishable from undeformed material from the same part and from pristine material by NMR spin-echo, NMR MOUSE and MRI protocols. The results of these studies have been interpreted in the context of studies of model materials of varying crosslink density. The areas of local deformation have been characterized by a reduction in the residual dipolar coupling, which is proportional to the crosslink density and in the non-network sol-fraction. These differences were likely present in these polymers at the time of production due to inefficient mixing. Additionally, both  $T_2$  weighted single point imaging (SPI) and  $T_2$  weighted MRI experiments have been used to map out the location of different crosslink densities, ultimately determining the quality or homogeneity in silicone components.

**Keywords:** Polymer degradation, NMR, MRI,  $T_2$  measurements, NMR MOUSE

\*Corresponding author. Tel: +1-925-423-4991, Fax: +1-925-422-5565.

†Current address: Dept. of Chemistry, Univ. of California, Santa Barbara, CA 93106  
*E-mail address:* maxwell7@llnl.gov (R. S. Maxwell).

# 1. Introduction

Elastomeric engineering parts, such as those employed in aerospace applications, can be subject to complex and harsh aging conditions including complex strain fields. When combined with structural heterogeneities due to processing inefficiencies, the result can be complex, heterogeneous aging of parts. This dramatically complicates lifetime estimates or system models for component performance. We have noted that engineering components constructed from a commercially available silicone elastomer subject to high degrees of compressive strain have been observed to contain small areas of permanent deformation upon return from service, as shown in Figure 1. These components have been traditionally produced in large batches and as a result, they are often subject to local volumes of lower or higher crosslink density or filler content. This is perhaps due to inefficiencies in the mixing process. In high strain environments, these volumes may be more subject to permanent set during the lifetime of the part.

Nuclear magnetic resonance (NMR) spectroscopy is routinely used to investigate structural and dynamic properties of polymers<sup>1</sup> and has found extensive use in the investigation of the effects of long-term exposure to chemically, thermally, or radioactively harsh environments on polymeric materials. NMR parameters such as transverse ( $T_2$ ) relaxation rates and residual dipolar coupling constants have been correlated with other chemical and mechanical tests such as DSC, GPC, and DMA to determine preliminary service lifetimes in a variety of polymers.<sup>2-5</sup> NMR offers the advantage of being able to probe simultaneously structure and dynamics *in situ*, in controlled environments, on samples of various shapes. Changes in chemical structure can be measured directly from changes in chemical shifts. In addition, changes in

crosslink density can be inferred from the resulting effects on the polymer sequential dynamics directly measurable from the NMR data. For example, the effects of  $\gamma$ -radiation on siloxane polymers has been shown to lead to changes in crosslink density as determined by  $T_2$ ,  $T_{1\rho}$ , and  $T_1$  relaxation times, as well as multiple quantum growth rates.<sup>5</sup> For example, Charlesby reported changes in  $T_2$  as a function of radiation dose for linear, uncrosslinked PDMS three decades ago.<sup>6</sup> In addition, Maxwell et al. have demonstrated the application of spin-echo, dipolar correlation effect spectroscopy, and multiple quantum methods to the characterization of radiation damage in complex, filled engineering silicones, including the synergistic effects of radiation and tensile strain.<sup>7</sup>

Standard high field NMR methods, however, are ill suited to provide non-destructive two or three dimensional maps of part structure due to production or aging heterogeneities. One method currently in use is unilateral relaxometry with the NMR MOUSE (MOBILE Universal Surface Explorer). Originally commercialized for the tire industry as an analytical tool for determining defect sites, the NMR MOUSE is a transportable, inexpensive and easy to use system based on the principles of NMR.<sup>8</sup> The MOUSE is currently used to determine mechanical properties of polymers,<sup>9-12</sup> fat content of dairy products,<sup>13</sup> and is even used in the preservation of artifacts such as historical papers and ancient stone ruins.<sup>14</sup> The MOUSE uses the same principles of traditional NMR spectroscopy, but since only relaxation information is obtained, the normal high resolution that is typically required for complete structural analysis is not needed and inhomogeneous static ( $B_0$ ) or excitation ( $B_1$ ) magnetic fields can be employed to significantly reduce the required foot print of the spectrometer.

MRI offers the ability to obtain a spatial map of the crosslink densities, which can be correlated to the overall structural inhomogeneity within the polymer materials.<sup>15</sup> MRI techniques have been employed to examine material properties, including, but not limited to, molecular motion, cross-link densities, the kinetics of crosslinking curing, rubber vulcanization, curing times for thermosetting polymers, and copolymer desiccation of elastomers.<sup>16-22</sup> Several reviews also exist on MRI techniques of materials, including polymers.<sup>16,17</sup> Unlike the MOUSE, MRI technique can obtain a spatial three dimensional image or map of polymer properties.

Engineering components manufactured from DC745, a commercial silicone available from Dow Corning, subject to high strain have been observed to be subject to local areas of permanent set, as shown in Figure 1. These areas have not been correlated to areas of higher local strain and efforts to reproduce this damage in the laboratory by deliberately over straining parts produced in small batches have failed. This data suggests that chemical heterogeneity in the original pads is the likely cause. It is our belief that these structural heterogeneities occur due to incomplete mixing during the production processes. The areas of chemical heterogeneity are then more susceptible to permanent set during service life. In this paper, we investigate the use of high resolution NMR, Magnetic Resonance Imaging (MRI) and the NMR MOBILE Universal Surface Explorer (MOUSE) as diagnostic tools for the identification of the defect sites as well as to perform a preliminary investigation into the exact nature the deformation.

## **2 Experimental Details**

### **2.1 DC745 Polymer**

DC745 was obtained from Dow Corning as Silastic<sup>®</sup> 745U and crosslinked with 0.55 wt% peroxide curing agent. Additional control samples were obtained by varying the curing agent concentration. A number of samples which were deformed during their service life were tested in addition to artificially aged samples. For the aging studies, samples were exposed to a <sup>60</sup>Co source (1.2 MeV, 500 kRad/hour) for the appropriate time required to achieve a dose range from 0-250 kGray. For high resolution NMR experiments, ~1 mm samples were cut and placed in a 5 mm NMR tube and placed in the center of the RF coil. Samples for the NMR MOUSE experiments were either ~1 cm x 1 cm pieces placed in the center of the surface coil or intact polymer pads placed on top of the MOUSE detection surface. MRI studies used excised samples of ~1 cm x 2 cm which were placed in the center of the RF coil.

## 2.2 High resolution NMR

Traditional <sup>1</sup>H spin echo experiments<sup>23</sup> were performed on a Bruker DRX 500 NMR spectrometer with a <sup>1</sup>H frequency of 500.09 MHz and a Bruker 5 mm TBI solution state probe. 90° pulse lengths of 6 μs and recycle delay times of 6 sec were used, and echo delays were varied from 0-15 ms. Echo intensity curves were plotted on a logarithmic scale and fit to a two-component decay curve representing a Gaussian decay in the presence of anisotropic motion due to topological constraints and an exponential decay representing the decay in the absence of motion<sup>3,7,24</sup>

$$E(t) = X_a \exp\left(-\frac{2t}{T_2} - \langle \Omega_d^2 \rangle \tau_c^2 \left[ \exp\left(\frac{t}{\tau_c}\right) + \frac{t}{\tau_c} - 1 \right]\right) + X_b \exp\left(-\frac{2t}{T_2}\right) \quad (1)$$

where  $t$  is the echo pulse spacing,  $T_2$  is the transverse relaxation time,  $\tau_c$  is the correlation time for the residual dipolar couplings,  $\langle \Omega_d \rangle$ .

### 2.3 NMR MOUSE Profiles of DC745 Polymer

Static, uniaxial NMR relaxometry experiments were performed using spin-echo decay curves obtained via a Carr-Purcell-Meiboom-Gill<sup>25</sup> pulse sequence on an NMR Mobile Universal Surface Explorer (MOUSE) from Bruker Optics operating at 16 MHz. [Note that the MOUSE is now being sold commercially by Bruker Optics as the minispec ProFiler, while newer models of the NMR MOUSE with unique applications such as unilateral imaging are continually under development by Blumich et al.<sup>26</sup>] Schematics of the NMR MOUSE magnet unit are shown in Figure 2. The experimental parameters were set as follows: echo time of 0.25 ms with 1500 echoes times per experiment and 512 scans signal averaged per echo time. The echo times were systematically increased until the  $T_2$  remained consistent to avoid the interfering effects of  $T_{1\rho}$  in the CPMG experiment. The pulse attenuation, receiver gain, and recycle delay were set to 6 dB, 103 dB, and 1 s, respectively. Decay curves were fit to a two-component exponential decay

$$E(t) = A_1 \exp\left(-\frac{2t}{T_{2_1}}\right) + A_2 \exp\left(-\frac{2t}{T_{2_2}}\right) \quad (2)$$

using the Bruker software. Further data processing was performed with the Contin application from Bruker Optics, which uses an inverse Laplace transform to yield the distribution of  $T_2$  relaxation times.

### 2.4 MR Images of DC745 Polymer

All MRI experiments were performed on a Bruker Avance 400 MHz spectrometer equipped with a high-resolution Micro5 microimaging system with either a 25 mm rf coil or a 5 mm rf coil depending on the size of the sample. The 2-D MRI T<sub>2</sub> weighted Single Point Imaging (SPI) pulse sequence is shown in Figure 3. The resulting images had a Field-of-View (FOV) of 3.0 by 3.0 cm with a resolution of 0.234 mm/pixel by 0.234 mm/pixel. The excitation pulse length was 10 μs, the detection time was 204.16 μs, 2 averages were obtained, and the total experiment time was 8 minutes and 13 seconds. The slice thickness was 1 mm. The 2D T<sub>2</sub> weighted NMR pulse sequence is shown in Figure 4. For these experiments the FOV was 6.0 cm by 6.0 cm with a resolution of 0.234 mm/pixel by 0.234 mm/pixel. The slice thickness was 2 mm. The 2D T<sub>2</sub> weighted MRI experiment were taken with a echo time of 10.25 ms, a repetition time of 1 s, one average, and a total time of 4 minutes and 16 seconds. For the samples exposed to γ-radiation, 2D T<sub>2</sub> weighted NMR experiments were performed with a Field-of-View (FOV) of 2.15 cm by 2.15 cm with a resolution of 0.168 mm/pixel by 0.168 mm/pixel. The slice thickness was 2 mm. The 2D T<sub>2</sub> weighted MRI experiment was taken with an echo time of 8 ms, a repetition time of 1 s, 4 average, and a total time of 8 minutes and 34 seconds.

## **3. Results and Discussion**

### **3.1 NMR MOUSE Profiles of DC745 Polymer**

Samples for traditional spin-echo NMR analysis were excised from the good and damaged sections of used pads and investigated. Results of the spin-echo experiments

are shown in Figure 5a and revealed significant differences in relaxation behavior. For both samples, the decay curve was initially characterized by considering a two component relaxation function, with the shorter decay representing network polymer chains and the longer decay representing the more mobile non-network sol fraction and dangling chain ends.<sup>24</sup> Initial observations of the decay curves indicated that while the sol fraction seemed to increase with damage, a slight change in the rates occurred in the more rapidly decaying sections representing the less mobile portions of the polymer network. The effective transverse relaxation time  $T_{2e}$ , which was obtained by subtracting out the long component and measuring the time the decay curve takes to decay to the value of  $1/e$ , was found to be 2.11 ms for the undamaged pad and 2.16 ms for the damaged pad. While a slight increase in  $T_{2e}$  was observed, the difference is negligible and indicates that the damage is occurring in the more mobile sol component of the polymer as opposed to the highly entangled portion of the polymer.

More thorough analyses of the decay curves were achieved by quantifying the residual dipolar couplings. In an ideal case, dipole-dipole interactions are typically averaged out through isotropic motions in the sample; however, topological constraints such as polymer crosslinking or network entanglements introduce anisotropic restrictions to these motions which do not completely average out the couplings on the NMR timescale. The remaining couplings are known as residual dipolar couplings,  $\langle \Omega_d \rangle$ , and their effects can often be observed in spin-spin relaxation behavior. The non-exponential decay seen in the first portions of the curves has been observed previously in silicone elastomers and is a consequence of the residual dipolar couplings.<sup>24</sup> To incorporate these effects, both curves underwent a least squares fit to a two-component decay according to

equation (1), above, to obtain the  $T_2$ ,  $\langle \Omega_d \rangle$ , and  $\tau_c$  values. The fits are shown in Figure 5a as the solid and dashed lines for the undamaged and damaged sections, respectively. The  $T_2$  relaxation time was determined to be 4.91 ms for the undamaged pad and 5.18 ms for the damaged pad, indicating a relative increase in mobility of the sample. Likewise, the residual dipolar coupling was observed to decrease from 677.7 Hz, with a correlation time of 1.70 ms, to 595.7 Hz with a correlation time of 2.12 ms, again corresponding to an increase in mobility. The most drastic change observed, however, is that the relative fraction of the slow component increased in the damaged sample. This indicates that the the damage causes a decrease in the fraction of the immobile phase either by chain scission or a reduction in the number of entanglements in the immobile phase.

Results of unilateral relaxometry via the NMR MOUSE on damaged and undamaged sections of an intact pad are shown in Figure 5b and Figure 6. In Figure 5b, the CPMG echo decay curves for the damaged (open squares) and undamaged (grey diamonds) sections of an intact pad are shown. The white and black lines are the results of a standard biexponential fit to equation (2) for the damaged and undamaged sections, respectively. While a two-component echo was again observed at low field, the longer experimental time required by the CPMG experiment reduced the signal from the fast component and produced a signal comprised primarily of the slow component (longer  $T_2$  time from the sol component). Additionally, the decay curves did not display the nonexponential behavior in the early time points seen in the high field data, so the data was not analyzed to account for residual dipolar couplings. For these reasons, only the long  $T_2$  component is shown in Figure 6 and considered hereafter. In this figure, the Contin  $T_2$  distribution plots are shown for the damaged and undamaged portions of an

intact pad. Since the surface coil on the MOUSE only penetrates a small distance into the polymer pad (the signal decreases by ~50% at a distance of 1 mm and ~90% by 2 mm), scans were run on both the top and bottom of the pad. If the defect is only in one portion of the pad and not present in the entire thickness of the pad, the changes in  $T_2$  might not be observable if only one side was scanned. As can be seen in Figure 6, distinct changes ( $T_2$ (damaged) = 75 ms;  $T_2$ (pristine) = 95 ms) were more observable in the top section of the polymer, indicating that the defect does not in fact go through the entire depth of the pad. (Figure 6 includes the data for replicate runs to demonstrate the reproducibility of the method.) It is important to note that the exact values of the  $T_2$  time cannot be directly compared when measured at different magnetic fields. In the low field case, the  $T_2$  relaxation time was nearly an order of magnitude larger than that obtained at high field. Since different experimental procedures (CPMG vs. traditional spin echo experiment) and parameters were used, the low field data can be quantitatively compared only with other low field data obtained with the same parameters and not with data obtained at different fields or using different experiments. However, it is interesting to note that the  $T_2$  value obtained from the damaged area of the pad is lower than that from the normal section of the pad. This observation is contrary to the high field NMR observation that the  $T_2$  increases with damage. One potential reason for this discrepancy is that the MOUSE is only detecting surface effects, while the high field NMR spectrometer detects the bulk properties of the sample. It is also possible that the surface of this polymer possesses structurally unique properties that are most affected by high load in service. Most importantly, as has been pointed out in other studies, care must be taken with making quantitative assessments of changes in crosslink density from spin-echo

methods.<sup>27,28</sup> The spin-echo methods are prone to contributions from dynamics over many decades of time scales and the effects of local field gradients produced by internal voids and filler particles.<sup>29</sup> Molecular dynamics experiments have shown that voids are created in these systems when subject to high levels of mechanical strain.<sup>30</sup> Both these effects have a complex dependence on the external magnetic field. In fact, a similar reversal of trends going from high field to low field analysis has been observed in styrene-butadiene rubbers.<sup>28</sup> This reversal certainly warrants more investigation, including in-depth analysis of the magnetic field dependence of the relaxation processes, sub-surface analysis with the MOUSE as well as low-field multiple quantum experiments which have been shown to be more selective to network structure and dynamics and reveal important information about polymer-filler interactions.<sup>31,32</sup>

To gain further insight into the dependences observed by the NMR MOUSE on the damaged and undamaged pads, we investigated a series of model materials: a) samples prepared with a lower concentration of peroxide catalyst, in this case 1/10 the normal catalyst amount and b) samples where the crosslink density has been modified by exposure to ionizing radiation (1.5 MeV gamma). Though the materials studied here were produced via traditional catalytic peroxide curing agents, the 1/10 fraction of the nominal agent was verified to produce a material with both lower crosslink density (via solvent swelling) and hardness (by DMA). The NMR MOUSE studies (not shown here) on these samples have shown that there is indeed a ~20 ms decrease in  $T_2$  relaxation time with the reduction in peroxide, with sufficient resolution between the two peaks. This trend, again, is opposite what one would expect from both high field studies and from theoretical expectations, but agrees qualitatively with the results from the damaged vs.

undamaged pads. These results of the variable catalyst study and the agreement with the data from the damaged pad suggest that there are fundamental dependencies of the curing process with both polymer-filler interactions and crosslinking processes.

Figure 7 shows the  $T_2$  distributions obtained by the MOUSE as a function of dose for the irradiated samples. The average  $T_2$  relaxation time was observed to decrease from 107 ms to 93 ms with increasing dose, indicating an increase in crosslink density. Interestingly, this trend is consistent with previous observations of radiation-induced crosslinking by high-field NMR and other mechanical methods and solvent swelling techniques,<sup>3-5,7</sup> Clearly, a different degradation mechanism is present in the case of radiative degradation than that observed in the damaged pads and the variable catalyst study.

Preliminary investigations of the field dependence of  $T_2$  times was performed using a Bruker minispec NMR spectrometer with a  $^1\text{H}$  NMR frequency of 19.95 MHz and the same experimental parameters as with the NMR MOUSE. The same samples tested on the NMR MOUSE were tested at a slightly higher, more homogeneous field and showed similar trends, namely that a damaged pad showed a lower  $T_2$  value than a good pad, decreasing peroxide catalyst levels showed decreasing  $T_2$  times, and radiative degradation resulted in decreasing  $T_2$  times with dose. These agreements indicate that the lower applied external magnetic field affects the NMR results more significantly than the external magnetic field gradients present in the NMR MOUSE system. Again, the field dependence certainly warrants more investigation, including variable field experiments to determine at which field the reversal occurs and low field multiple quantum investigations, which have been shown to be more sensitive to changes in network

structure and dynamics and reveal important information about polymer-filler interactions.<sup>31,32</sup> However, it is important to note that for the context of this investigation, the use of the NMR MOUSE is meant solely as a qualitative diagnostic tool for the detection of local deformations in polymeric materials. While these results are certainly intriguing, a detailed analysis of these mechanisms and their field dependence is beyond the scope of this investigation.

### **3.2 MR Images of DC745 Polymer**

Given the limited ability of the commercial NMR MOUSE equipped only with a surface coil to provide depth profiles of the damage, we employed MRI methods. MRI is an ideal method to develop a 3D map of the structure homogeneity within the polymer materials given the sensitivity of the NMR observable  $T_2$  to the segmental dynamics and thus polymer network structure. We have analyzed both model materials and damaged and undamaged field return samples. Two methods were employed: Single Point Imaging (SPI)<sup>33-35</sup> and traditional  $T_2$  weighted MRI.<sup>36</sup> SPI was used because it enhances in the difference in very short  $T_2$  relaxation times. This technique is only useful for  $T_2$  relaxation times on the order of 50  $\mu$ s to 1 ms. Since each single complex time domain data point is collected after one individual excitation and the time between the excitation and the detection stays constant for each data point, this method is not sensitive to chemical shift evolution, field inhomogeneity and local susceptibility changes in the object. However, this technique can efficiently distinguish between two very fast  $T_2$  relaxation times and suppresses slow  $T_2$  relaxation times. The 2-D MRI  $T_2$  weighted SPI

on two model DC745 samples are shown in Figure 8. The polymer on top was prepared with the nominal catalyst level and the polymer on the bottom was prepared with 1/10<sup>th</sup> the catalyst level. The contrast parameter is  $T_2$  relaxation time with higher signal intensity indicating higher  $T_2$  and thus higher mobility of the polymer network, which correlates to a lower crosslink density. As expected, this figure shows that the polymer sample prepared with nominal catalyst levels has a lower signal intensity and lower  $T_2$  relaxation time, i.e. a lower mobility of the polymer network, which correlates to higher crosslink density. On the other hand, the polymer sample prepared with 1/10<sup>th</sup> the catalyst level, (bottom of Figure 8b) has a higher signal intensity and a higher  $T_2$  relaxation time, i.e. a low crosslink density.

As observed in the high field spin-echo experiments in Figure 5, the materials were characterized by both a short and a long relaxation time component.  $T_2$ -weighted MRI experiments are potentially more efficient for distinguishing polymers with crosslink densities associated with slow  $T_2$  relaxation times.  $T_2$  weighted MRI is typically used in clinical applications to detect pathological tissues due to the elongated  $T_2$  relaxation times; for example, high signals intensities occur in tumors, which allows clinicians to distinguish between tumors and soft-tissues.<sup>36</sup> A similar experiment can be used to distinguish polymers with different crosslink densities and to determine if inhomogeneities exist within the material. The 3D MRI results from the  $T_2$  weighted experiments on samples prepared with nominal catalyst levels, 1/2 nominal catalysts levels, and 1/10<sup>th</sup> nominal catalyst levels are shown Figure 9. Here the sample with the highest crosslink density is on the left and the sample with the lowest crosslink density is on the right. The figure includes a physical picture of the DC745 polymer, a 3D  $T_2$  weighted

MR Image of this DC745 polymer, a 2D slice of  $T_2$  weighted MR Image of DC745 polymers, and 1D slice showing the image intensity, proportional to  $T_2$ , providing quantitative values of the crosslink density profiles of the polymers. In the 3D, 2D, and 1D images, the signal intensities of the three slices increase left to right, indicating a decrease in crosslink densities across the three samples. The intensity data shown in this slice indicates that the nominal and  $\frac{1}{2}$  nominal catalyst level samples are characterized by similar  $T_2$  values and the sample prepared with  $1/10^{\text{th}}$  nominal catalyst level is characterized by a  $T_2$  value that is  $\sim 50\%$  higher. This data is consistent with high field NMR reported above and with solvent swelling data.

The  $T_2$  weighted MRI images of polymers that were exposed to different doses of radiation are shown in Figure 10. This figure also shows the  $T_2$  profile of the MRI image through a randomly selected slice shown in the figure. In this MRI image, the contrast parameter again, is the  $T_2$  relaxation time, with higher signal intensity indicating higher  $T_2$  and thus lower crosslink density. The MRI data clearly displays the same trend as the high resolution NMR and the unilateral NMR relaxometry, as well as solvent swelling observations, where  $T_2$  decreases and crosslink density increases with increasing radiation dose.<sup>17</sup> These MR Images of irradiated DC745 polymer have interesting features. Around the surface of the polymer for both the pristine and irradiated samples, there is a clear lower signal intensity, which indicates higher crosslink density; than on the interior of the polymers, potentially caused by curing effects or magnetic susceptibility changes between the air and polymer interfaces. Since the surface coil on the MOUSE only penetrates a small distance into the polymer pad, the MOUSE

technique using this coil alone might be highly problematic in determining crosslink densities in the interior of the polymer pads. To eliminate surface effects that may lead to NMR signal distortions, use of subsurface coils with different penetration depths is necessary. These investigations are currently underway in our laboratory.

To show how MRI techniques can be used to obtain crosslink densities of a non-ideal damaged section and a pristine section of a DC745 polymer pad, we performed 2D  $T_2$  weighted MRI experiments on these pads. The 2D  $T_2$  weighted MR Images are shown in Figure 11. The contrast parameter is  $T_2$  relaxation time. The undamaged pad section is characterized by a fairly uniform  $T_2$  throughout the material part with exception of the lower signal intensity at the surface. Consistent with the high field data shown above, the damaged pad was characterized by areas of brighter signal due to increased  $T_2$  relaxation time, or higher mobility of the polymer network. It is important to note that brighter signals are present in patches in the interior of the polymer pads, which may be due combined effects of cross-link density and compression set. The MRI data shown here confirms that the damaged DC745 pads, after service, can be described by heterogeneities in the mobility of the polymer network through the pad. Areas of the pads without the heterogeneity do not seem subject to this deformation.

Figure 12 shows that high resolution images are not necessary in locating these deformations. In this figure,  $T_2$  weighted MR Images of DC745 polymers were obtained at different resolutions, including (a) 156  $\mu\text{m}/\text{pixel}$ , (b) 312  $\mu\text{m}/\text{pixel}$ , (c) 624  $\mu\text{m}/\text{pixel}$ , and (d) 1.25 mm/pixel. The total time for each image was 4 minutes, 2 minutes, 1 minute, and 30 seconds, respectively. At 156  $\mu\text{m}/\text{pixel}$  resolution, the location of the defects in the polymer pads can be clearly be determined. However, reasonable identification of

heterogeneities can be obtained with either 624  $\mu\text{m}/\text{pixel}$  or 1.25 mm/pixel resolution. By using a less resolved MR Image, one can save hours in examining polymer pads for rapid production or screening. However, for obtaining more specific information, including precise locations of crosslink density heterogeneities, high resolutions might be needed.

## **4. Conclusions**

NMR-based techniques were used to detect heterogeneities in polymer mobility that may have led to areas of permanent deformation in service environments of high strain. Unilateral NMR relaxometry and high field NMR and MRI indicated that differences in  $T_2$  relaxation time clearly existed in excised damaged sections of deformed service pads. Experiments performed on model materials allowed us to baseline the NMR data on the deformed service material. MRI experiments were used to record the exact location of different mobilities of polymer networks, ultimately providing a 2D or 3D spatial map of the heterogeneity in the polymers components. MRI can also distinguish defects in the interior and on the surface of these polymer pads. While work is underway to determine the exact nature of the deformation in the polymer pads, both the NMR MOUSE and MRI can certainly be used to distinguish areas of permanent deformation in intact DC745 silicone pads.

## **5. Acknowledgements**

This work was performed under the auspices of the U.S. Department of Energy by the University of California, Lawrence Livermore National Laboratory, under contract # W-7405-ENG-48.

## 6. References

1. Schmidt-Rohr, K., Spiess, H.W. *Multidimensional Solid State NMR and Polymers*; San Diego: Academic Press, 1994.
2. Chien, A., Maxwell, R.S., Chambers, D., Balazs, B., LeMay, J. Characterization of radiation-induced aging in silica-reinforced polysiloxane composites. *J. Rad. Phys. Chem* 2000; 59: 493.
3. Maxwell, R., Balazs, B. Residual dipolar coupling for the assessment of crosslink density changes in  $\gamma$ -irradiated silica-PDMS composite materials. *J. Chem. Phys.* 2002; 116: 10492.
4. Maxwell, R., Balazs, B. NMR measurements of residual dipolar couplings for lifetime assessments in  $\gamma$ -irradiated silica-PDMS composite materials. *Nuc. Inst. Meth. Phys. Res. B* 2003; 208: 199.
5. Maxwell, R., Cohenour, R., Sung, W., Solyom, D., Patel, M. The effects of  $\gamma$ -irradiation on the thermal, mechanical, and segmental dynamics of a silica filled, room temperature, vulcanized polysiloxane rubber. *Poly. Deg. Stab.* 2003; 80: 443.
6. Charlesby, A. Radiation Effects in Macromolecules: Their Determination with Pulsed Nuclear Magnetic Resonance (NMR). *Rad. Phys. Chem.* 1985; 26: 463.
7. Maxwell, R.S., Chinn, S.C., Solyom, D., Cohenour, R. Radiation induced degradation in a silica-filled silicone elastomer as investigated by multiple quantum NMR. *Macromolecules* 2005; 38: 7026.
8. Eidmann, G., Savelsberg, R., Blumer, P., Blumich, B. The NMR MOUSE, a mobile universal surface explorer. *J. Mag. Res. A* 1996; 122: 104.
9. Kuhn, W., Klein, M., Wiesmath, A., Demco, D.E., Blumich, B., Kelm, J., Gold, P.W. The NMR MOUSE: quality control of elastomers. *Mag. Reson. Imaging* 2001; 19: 497.
10. Zimmer, G., Guthausen, A., Blumich, B. Characterization of crosslink density in technical elastomers by the NMR-MOUSE. *Solid State NMR* 1998; 12: 183.
11. Todica, M., Fechete, R., Blumich, B. Selective NMR excitation in strongly inhomogeneous magnetic fields. *J. Mag. Res.* 2003; 164: 220.
12. Guthausen, A., Zimmer, G., Blumer, P., Blumich, B. Analysis of polymer materials by surface NMR via the NMR MOUSE. *J. Mag. Res.* 1998; 130: 1.
13. Pedersen, H.T., Ablett, S., Martin, D.R., Mallet, M.J.D., Engelsens, S.B. Application of the NMR-MOUSE to food emulsions. *J. Mag. Res.* 2003; 165: 49.

14. Sharma, S., Casanova, F., Wache, W., Segre, W., Blumich, B. Analysis of historical porous building materials by the NMR-MOUSE. *Mag. Reson. Imaging* 2003; 21: 249.
15. Wallner, A.S., Ritchey, W.R. Applications of magnetic resonance imaging to ion-exchange resins. *J. Appl. Poly. Sci.* 1995; 57: 1.
16. Demco, D.E., Blumich, B. NMR imaging of materials. *Current Opinion in Solid State and Material Science* 2001; 5: 195.
17. Blumer, B., Blumich, B. NMR imaging of elastomers: A review. *Rubber Chem. Tech.* 2001; 70: 468.
18. Adriaensens, P., Pollaris, A., Vanderzande, D., Gelen, J., White, J.L., Dias, A.J., Kelchtermans, M. Critical analysis of network defects in cross-linked isobutylene-based elastomers by NMR imaging. *Macromolecules* 1999; 32: 4692.
19. Adriaensens, P., Pollaris, A., Kelchtermans, M., Gelen, J. Determination of the local cross-link density in polyisobutylene-based elastomers by NMR imaging. *Macromolecules* 2003; 36: 706.
20. Kuhn, W., Barth, P., Hafner, S., Simon, G., Schneider, H. Material properties imaging of cross-linked polymers by NMR. *Macromolecules* 1994; 27: 5773.
21. Kuhn, W., Barth, P., Denner, P., Muller, R. Characterization of elastomeric materials by NMR-microscopy. *Solid State NMR* 1996; 6: 295.
22. Cherry, B.R. Relaxation nuclear magnetic resonance imaging (R-NMRI) of PDMS/PDPS siloxane copolymer desiccation. *Polymer* 2004; 45: 5611.
23. Fukushima, E., Roeder, S.B.W. *Experimental Pulse NMR: A Nuts and Bolts Approach*; Reading, MA: Addison-Wesley Publishing Company, Inc., 1981.
24. Cohen-Addad, J.P. NMR and fractal properties of polymer liquids and gels. *Prog. NMR Spect.* 1993; 25: 1.
25. Meiboom, S., Gill, D. Modified spin-echo method for measuring nuclear relaxation times. *Rev. Sci. Instr.* 1958; 29: 688.
26. For the latest in NMR MOUSE development, please visit <http://www.nmr-mouse.de/>
27. Luo, H., Kluppel, M., Schneider, H. Study of filled SBR elastomers with NMR and mechanical measurements. *Macromolecules* 2004; 37: 8000.
28. Saalwachter, K. Artifacts in transverse proton NMR relaxation studies of elastomers. *Macromolecules* 2005; 38: 1508.
29. Kenny, J.C., McBrierty, V.J., Rigbi, Z., Douglass, D.C. Carbon black filled natural rubber. 1. Structural investigation. *Macromolecules* 1991; 24: 436.
30. Lacevic, N., Maxwell, R.S., Saab, A., Gee, R.H. Molecular dynamics simulations of ordering of polydimethylsiloxane under uniaxial stress. *J. Phys. Chem. B* 2005; in press.
31. Saalwachter, K., Ziegler, P., Spyckerelle, O., Haider, H., Vidal, A., Sommer, J.-U.  $^1\text{H}$  multiple-quantum nuclear magnetic resonance investigations of molecular order distributions in poly(dimethylsiloxane) networks: Evidence for a linear mixing law in bimodal systems. *J. Chem. Phys.* 2003; 119: 3468.
32. Saalwachter, K.  $^1\text{H}$  multiple-quantum nuclear magnetic resonance investigations of molecular order in polymer networks. II. Intensity decay and restricted slow dynamics. *J. Chem. Phys.* 2004; 120: 454.

33. Kennedy, C.B., Balcom, B.J., Mastikhin, I.V. Three-dimensional magnetic resonance imaging of rigid polymeric materials using single-point ramped imaging with T-1 enhancement (SPRITE). *Can. J. Chem.* 1998; 76: 1753.
34. Emid, S., Creyghton, J.H.N. High resolution NMR imaging in solids. *Physica* 1985; 128B: 81.
35. Fang, Z., Hoepfel, D., Winter, K. Application of single point imaging (SPI) to solid state materials. *Mag. Reson. Imaging* 2001; 19: 501.
36. Haake, E.M., Brown, R.W., Thompson, M.R., Vanderzande, D. *Magnetic resonance imaging: physical principles and sequence design*; New York: John Wiley & Sons, 1999.

## Table of Figures

**Figure 1:** Photo of damaged (left) and pristine (right) DC745 pad.

**Figure 2:** Schematic of MOUSE magnet unit, showing the  $B_0$  (black dashed) and  $B_1$  (red dashed) magnetic field lines and the DC745 sample (dark grey). The size of this unit is approximately 4 inches across.

**Figure 3:** Single Point Imaging (SPI) MRI pulse sequence for obtaining images biased toward short  $T_2$  ( $\mu\text{s}$ ) relaxation times.

**Figure 4:**  $T_2$  weighted MRI pulse sequence for obtaining images biased toward long  $T_2$  (ms) relaxation times.

**Figure 5:** (a) Echo decay curves with high field data points (x = damaged; circle = undamaged) and  $T_2$  curves (dashed = damaged; solid = undamaged), fit to equation (1). (b) Low-field CPMG echo curves in a damaged and pristine section of DC745. Solid lines are results of a biexponential fit to equation (2).

**Figure 6:** Results of replicate unilateral NMR relaxometry experiments for service DC745 components. Solid lines = undamaged areas; dashed lines = damaged areas. Experiments performed either by putting the MOUSE against the top or bottom of the component. The curves are the results of inverse Laplace transforms of the echo decay curves obtained by the NMR MOUSE, see text for details.

**Figure 7:** Results of unilateral NMR relaxometry for DC745 exposed to  $\gamma$ -radiation in air. The curves are the results of inverse Laplace transforms of the echo decay curves obtained by the NMR MOUSE, see text for details.

**Figure 8:** a) Visual picture of 2 DC745 samples (Top =nominal catalyst content and Bottom = 1/10th catalyst), compared to a dime. b) 2D  $T_2$  weighted SPI on the two DC745 samples. The contrast parameter is  $T_2$  relaxation time, with higher signal intensity (left image = white; right image = red) indicating higher  $T_2$ .

**Figure 9:** MRI derived 3D spatial maps of the crosslink densities DC745 polymers prepared with the nominal catalyst amount,  $\frac{1}{2}$  the catalyst level,

and 1/10<sup>th</sup> the catalyst level. a) A picture of DC745 polymers, compared to a quarter, b) 3D T<sub>2</sub> weighted MRI of DC745 polymers, c) 2D slice of T<sub>2</sub> weighted of DC745 polymers, and d) 1D slice of T<sub>2</sub> weighted of DC745 polymers, providing quantitative values of the crosslink density of a polymer.

**Figure 10:** 2D T<sub>2</sub> weighted MRI experiment on polymers exposed to different levels of radiation dose. The contrast parameter is T<sub>2</sub> relaxation time with higher signal intensity indicating lower crosslink density.

**Figure 11:** a) Visual picture of damaged section and pristine section of DC745, compared to a quarter. The 2D T<sub>2</sub> weighted MRI experiments of damaged section and pristine section of DC745. The contrast parameter is T<sub>2</sub> relaxation time, with higher signal intensity indicating lower crosslink density.

**Figure 12:** T<sub>2</sub> weighted MRI of DC745 polymers at different resolutions a) Matrix = 256 x 256, Resolution = 156μm/pixel, and total time = 4 min, b) Matrix = 128 x 128, Resolution = 312μm/pixel, and total time = 2 min, c) Matrix = 64 x 64, Resolution = 624μm/pixel, and total time = 1 min, and d) Matrix = 32 x 32, Resolution = 1.25mm/pixel, and total time = 30sec.

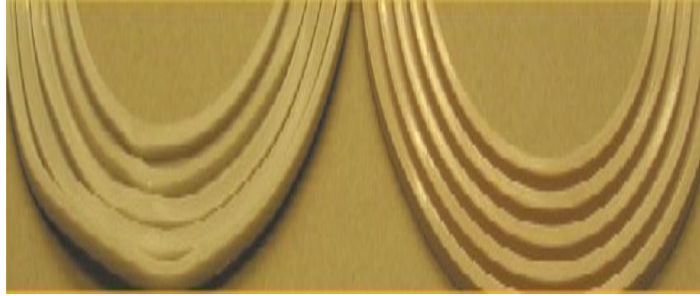


**Figure 1**

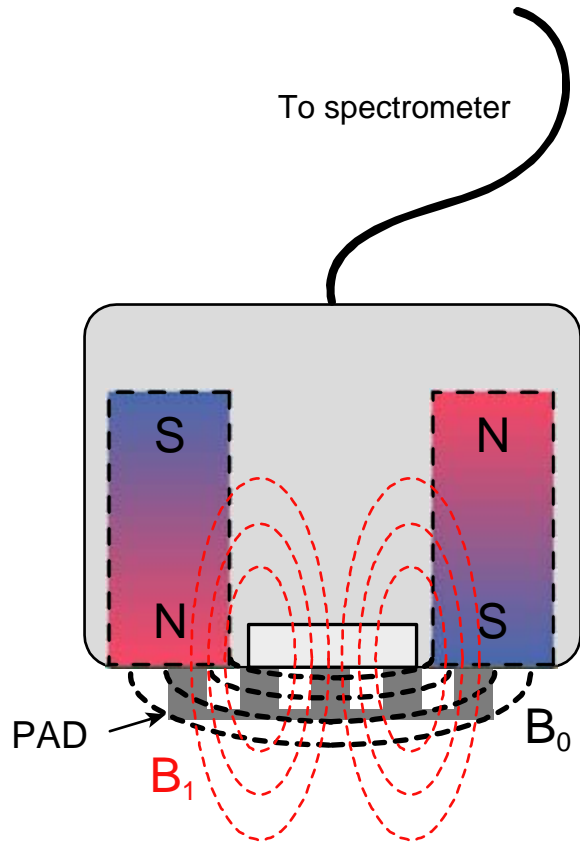


**Figure 2**

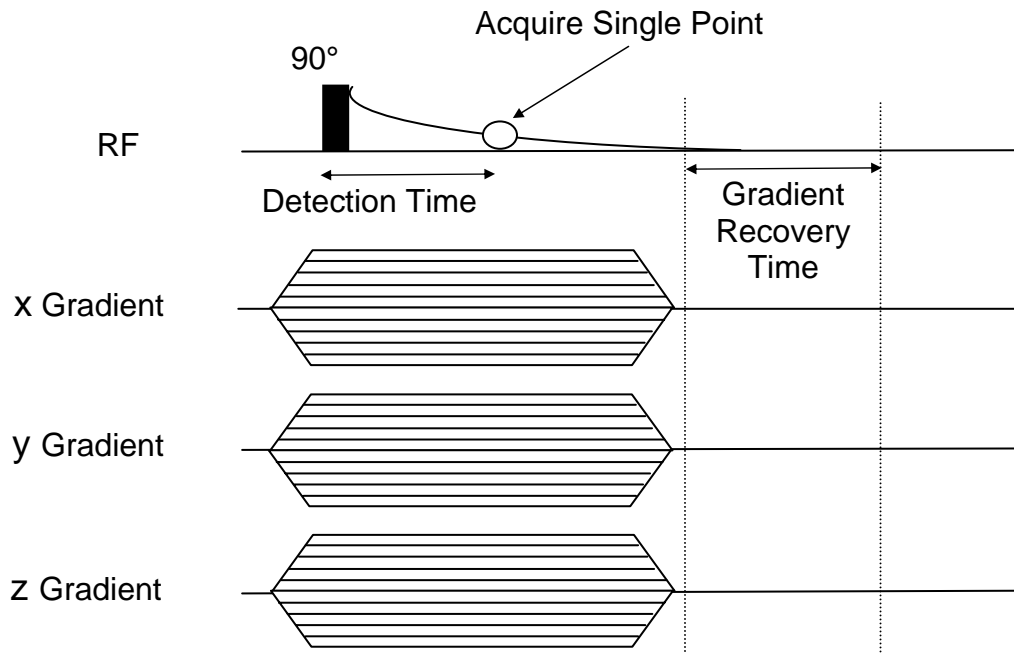


**Figure 3**

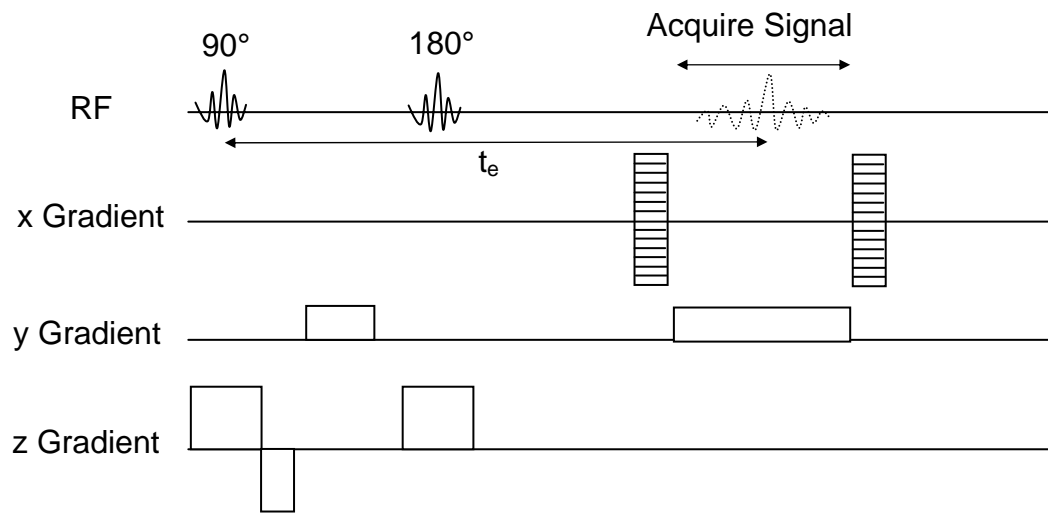
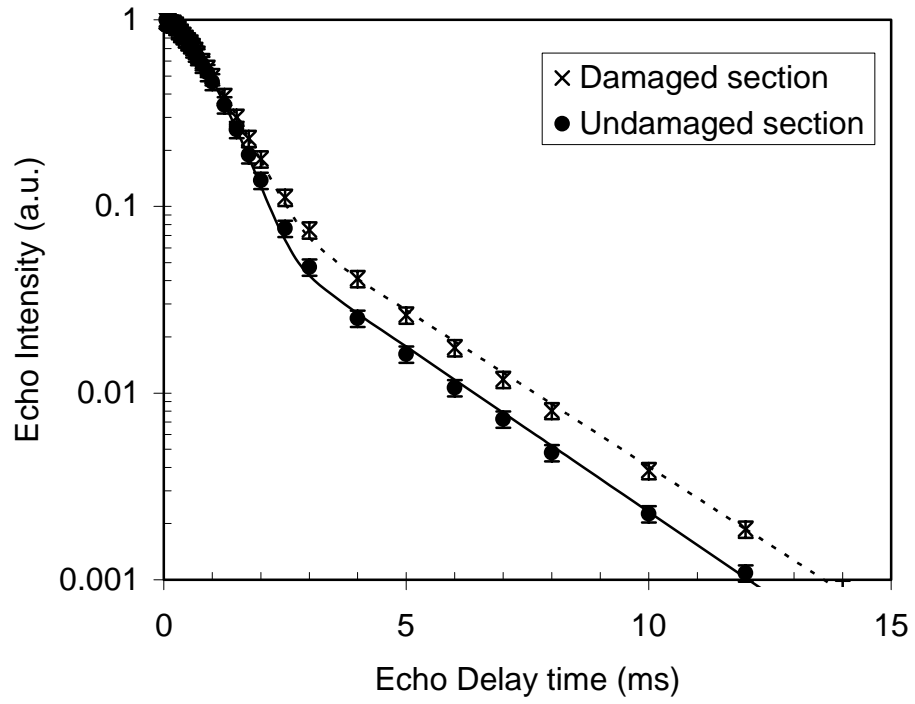


**Figure 4**

(a)



(b)

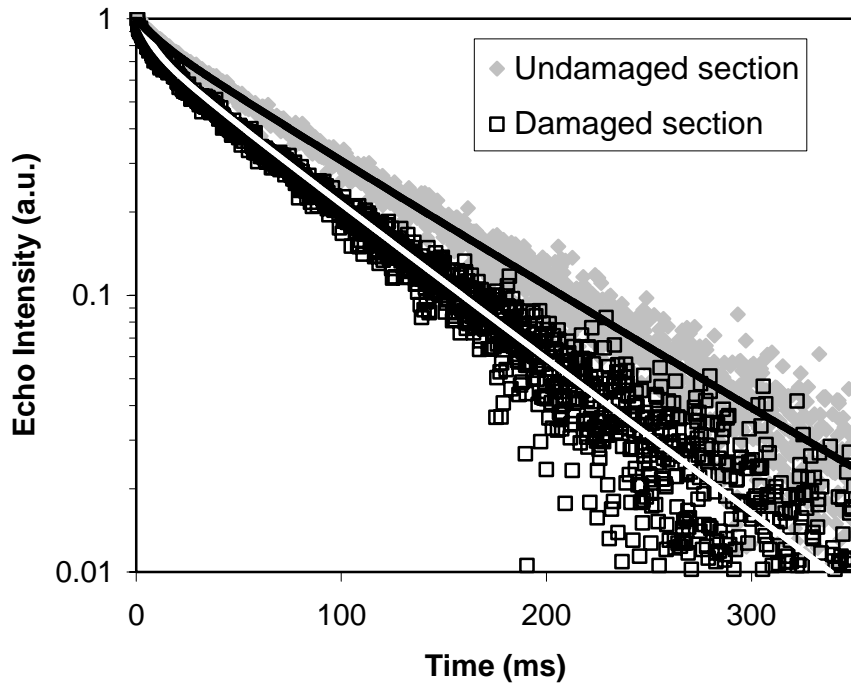
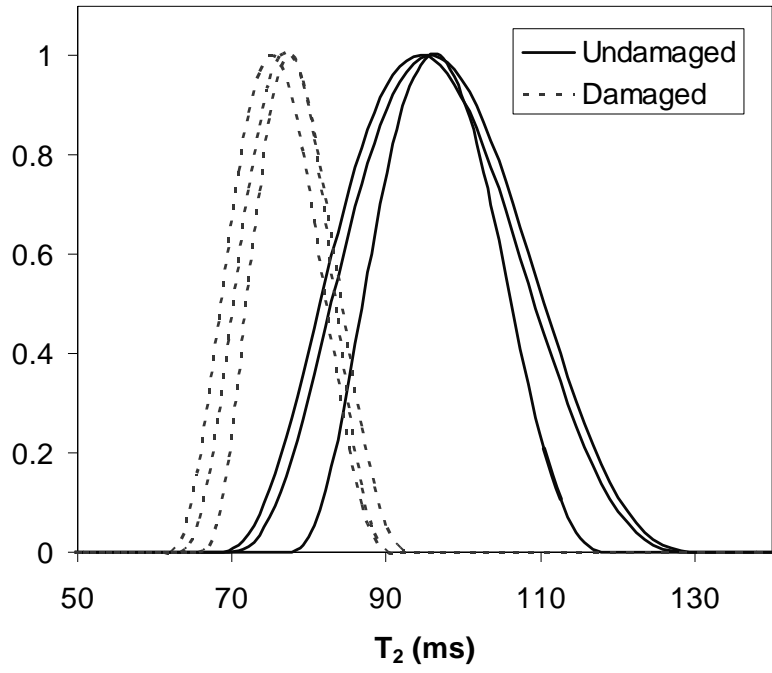
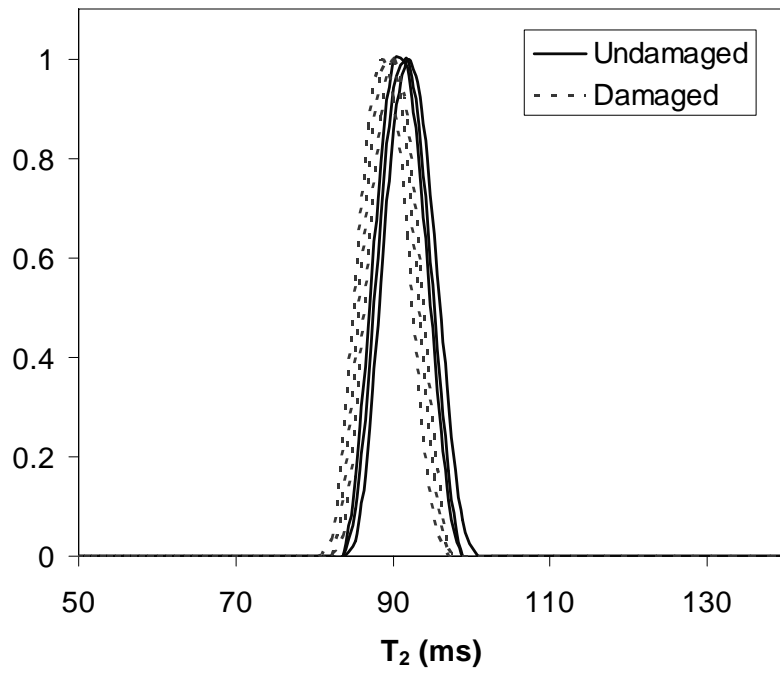


Figure 5

**Top**



**Bottom**



**Figure 6**

### DC745 Irradiation in Air

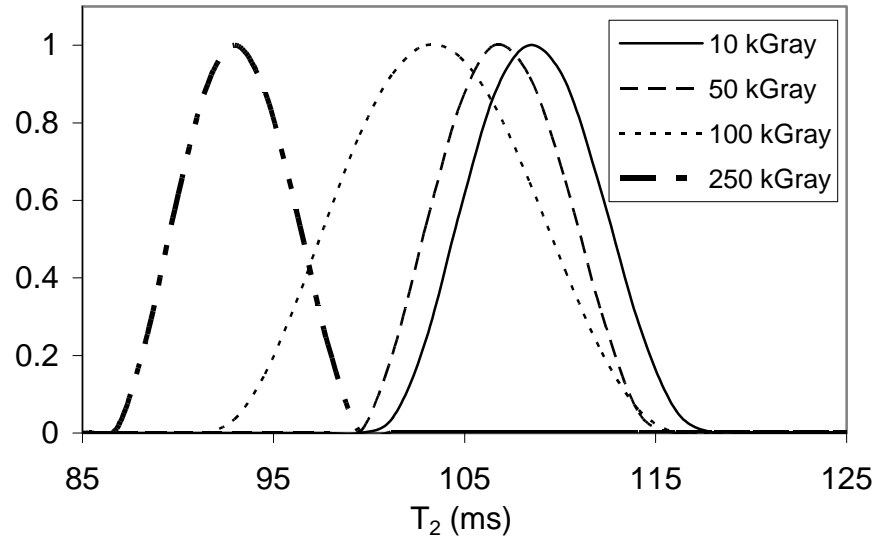


**Figure 7**

a)



b)

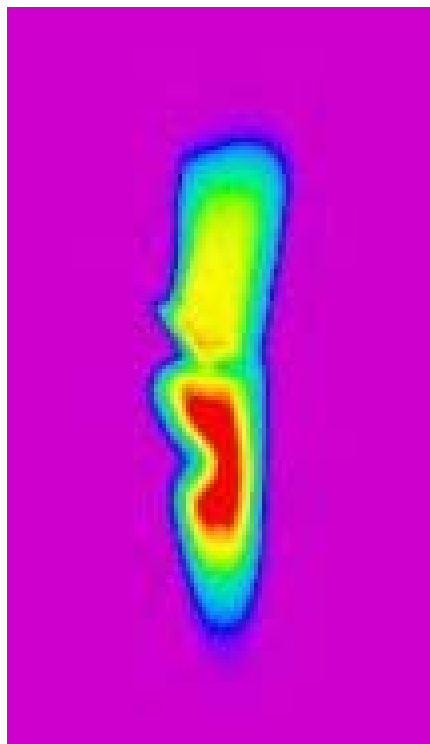
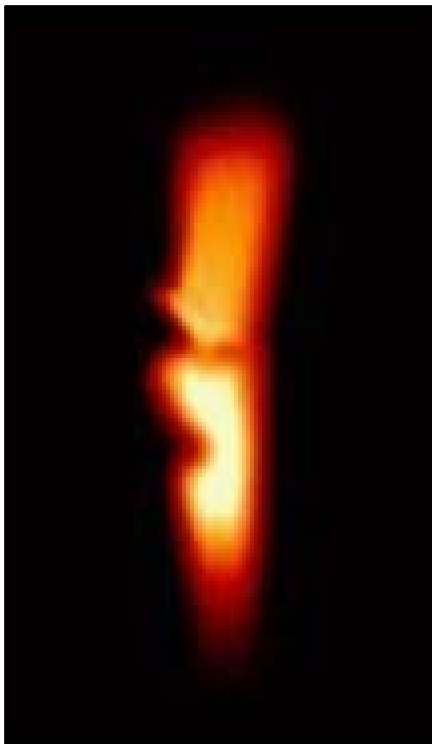


Figure 8

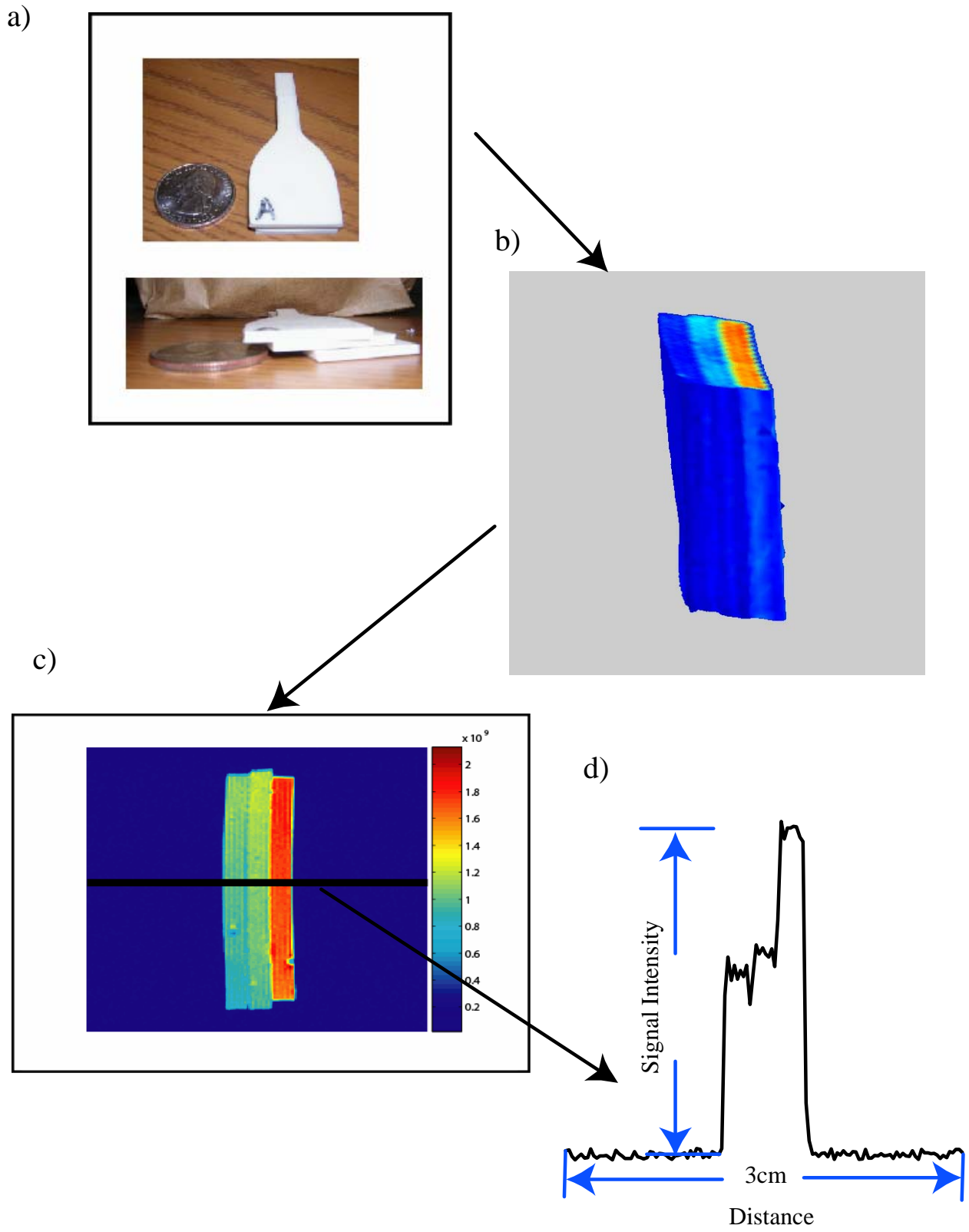
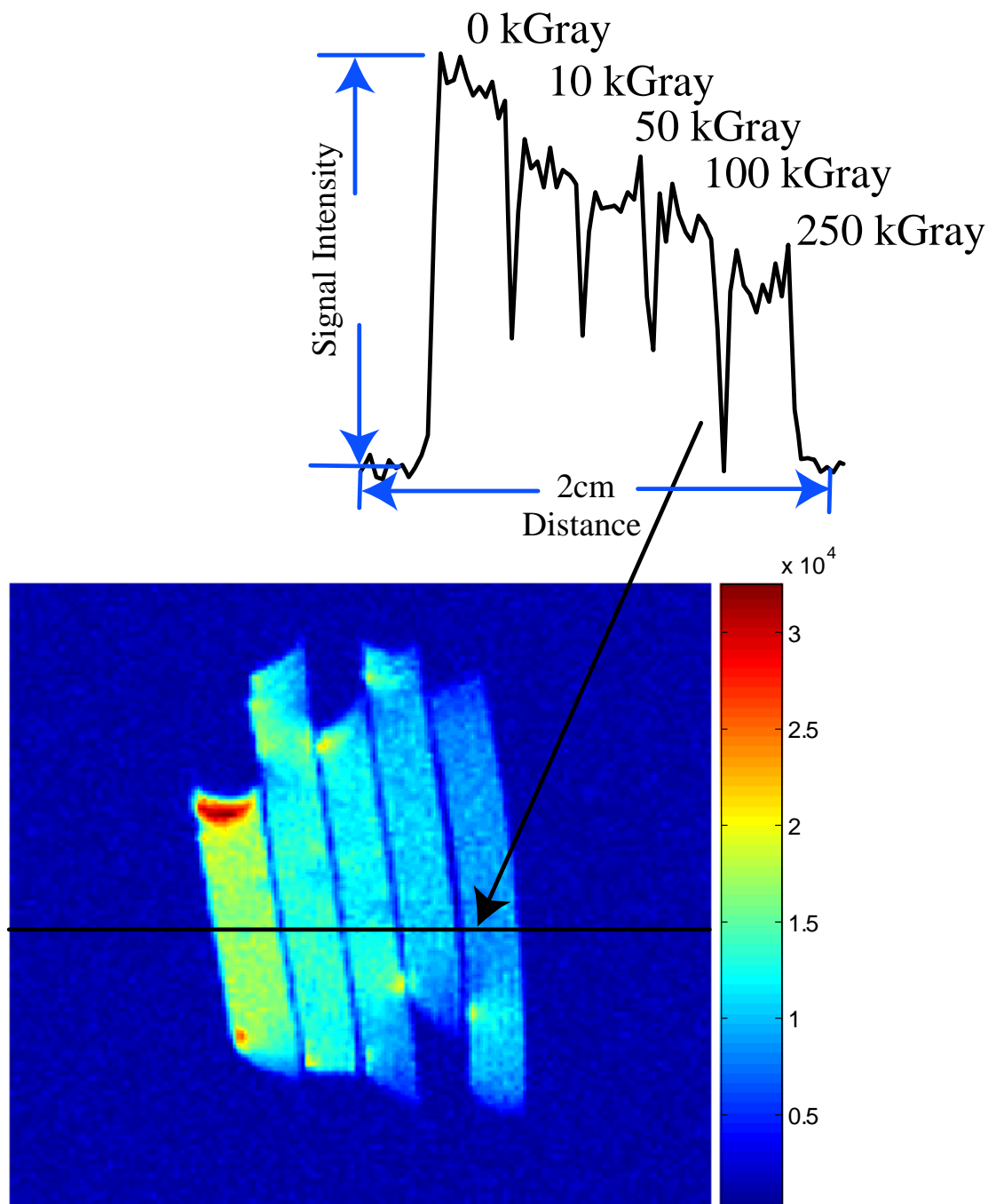


Figure 9



**Figure 10**

a)



b)

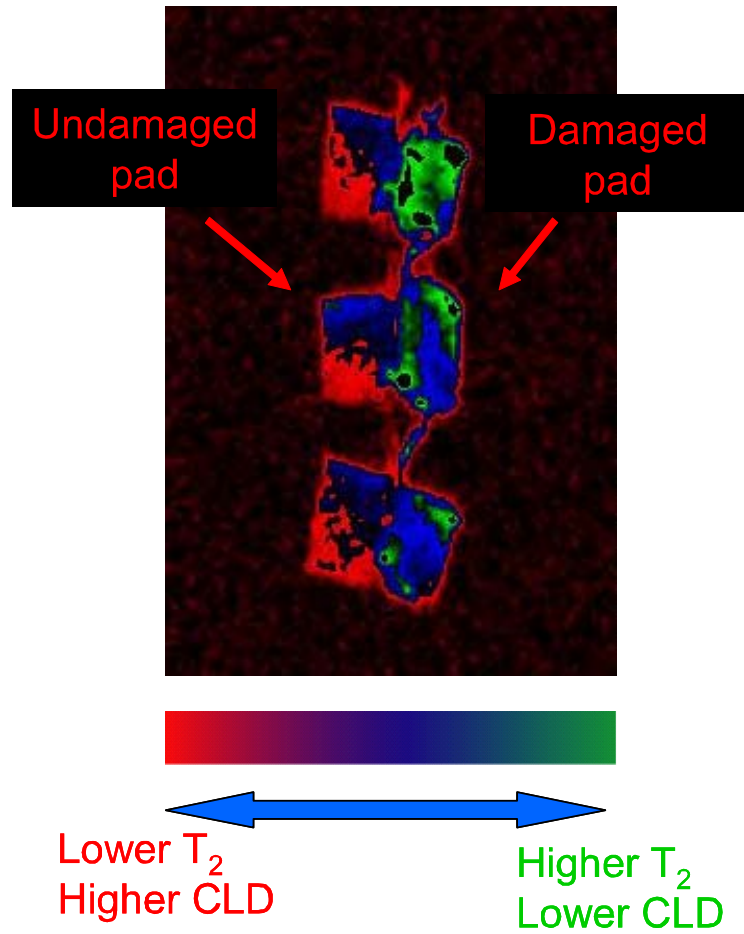
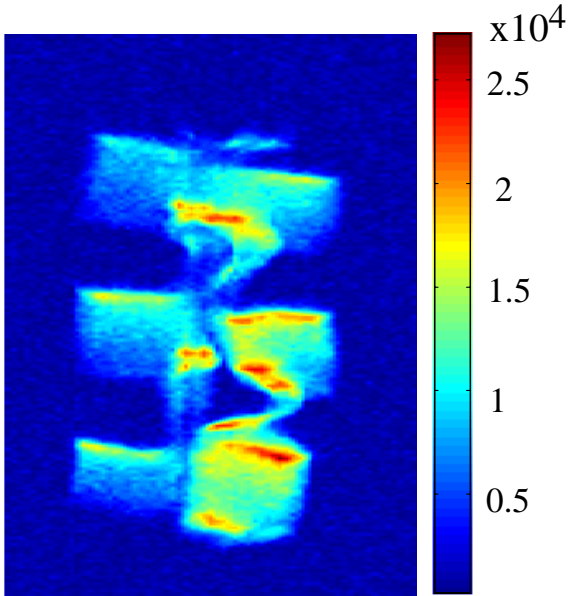
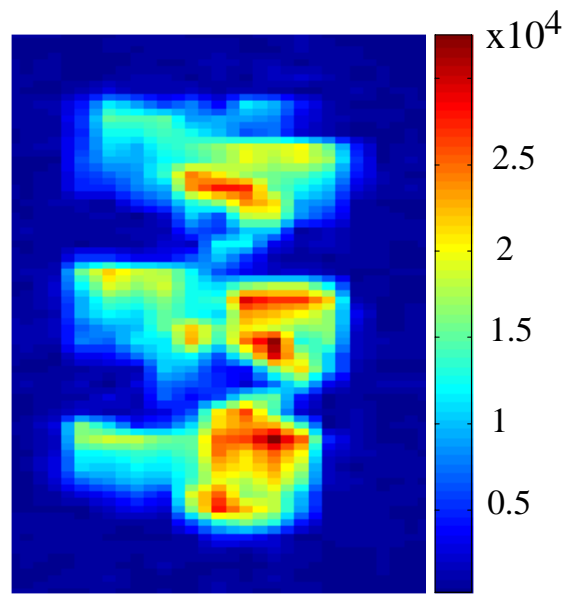


Figure 11

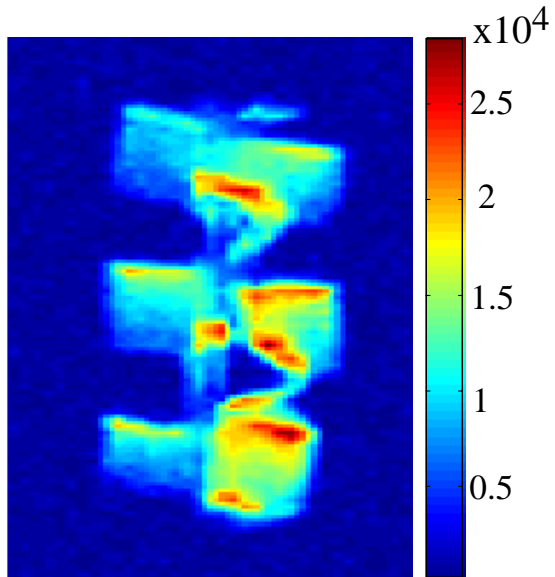
a)



c)



b)



d)

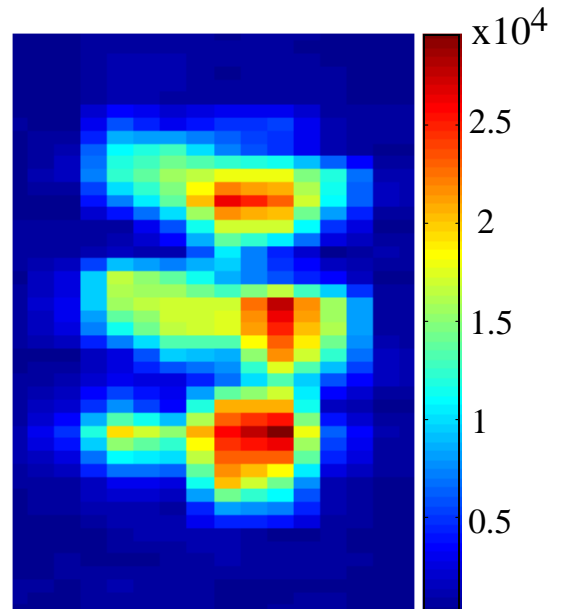


Figure 12